

# Quantum entanglement and Bell nonlocality in top-quark pair production at a photon linear collider

Seong Youl Choi<sup>1, a, e</sup> Dong Woo Kang<sup>1, b, e</sup> Jae Sik Lee<sup>2, c</sup> and Chan Beom Park<sup>2d, e</sup>

<sup>1</sup>*Department of Physics, Jeonbuk National University, Jeonju, 54896, Korea*

<sup>2</sup>*Department of Physics and IUEP, Chonnam National University, Gwangju 61186, Korea*

(Dated: March 13, 2026)

A photon linear collider, the two-photon collision mode of an  $e^+e^-$  linear collider, uses high-energy laser photons backscattered off the incoming electrons and positrons. The colliding-photon polarization is fully controllable through the polarizations of the initial electron and positron beams and laser photons. We investigate the impact of colliding-photon polarization on the observability of quantum entanglement in top-quark pair production at a photon linear collider. Constructing the spin density matrix of the  $t\bar{t}$  two-qubit system from the helicity amplitudes, we demonstrate that a photon linear collider is an ideal machine to probe quantum entanglement and Bell nonlocality across the broad phase space of the process.

## I. INTRODUCTION

At colliders, the *measurement* takes place when the polarized particles decay and quantum entanglement is accessible through correlations among particle spins [1]. The short lifetime of top quark,  $\tau_t \sim 10^{-25}$  s, is much shorter than the spin-correlation timescale of  $\sim 10^{-21}$  s, making it a good probe of quantum entanglement at colliders, owing to the simplicity and analyticity of the two-qubit quantum state. Quantum entanglement and Bell inequality violation in top-quark pair production at the LHC were first proposed in Refs. [2, 3]. Indeed, the ATLAS and CMS collaborations at the LHC have reported the observation of quantum entanglement with a significance exceeding  $5\sigma$  near the  $t\bar{t}$  production threshold [4, 5] and at high  $t\bar{t}$  invariant masses [6].

Quantum entanglement gives rise to the stronger spin correlations, than those expected in the classical theory, among the states which once interacted but, being separated spatially, cannot interact now. At colliders, the spin correlations are accessible through the distribution of the momenta of the final state into which the original particle decays [7]. The possibilities to probe quantum entanglement at colliders were first suggested in Refs. [8–11]. More recently, it was shown that quantum entanglement is experimentally accessible in the Higgs boson decays into charged gauge bosons [12], using two-qubit systems such as top-quark, tau-lepton and photon pairs [13], in the Higgs boson decay into tau leptons [14], in weak gauge boson production [15], and in  $B$  meson decays [16]. Since the ATLAS and CMS collaborations reported observation of quantum entanglement at the LHC, several proposals have appeared to measure quantum entanglement and Bell nonlocality at the LHC [17–24],<sup>1</sup> an  $e^+e^-$  collider [28–34], and a muon collider [35]. Other proposals target the Higgs boson decays into four fermions via two vector bosons [36] and the decay of neutral kaons into two and three pions [37]. For the current status of quantum entanglement and Bell nonlocality at colliders, we refer to Refs. [1, 38, 39].

In this work, we investigate quantum entanglement and Bell nonlocality in top-quark pair production at a photon linear collider (PLC),  $\gamma\gamma \rightarrow t\bar{t}$ . A PLC is the two-photon collision mode of an  $e^+e^-$  linear collider, using backscattered laser photons off the incoming electrons and positrons [40–47]. The capability of controlling the colliding-photon polarizations, combined with the clean experimental environment, makes a PLC an ideal machine to probe quantum entanglement and Bell inequality violation.

This paper is organized as follows. In Section II, we introduce the spin density matrix of a two-qubit system composed of two spin-1/2 particles and briefly review the four criteria for quantum entanglement and Bell inequality violation considered in this work. Section III is devoted to developing the spin density matrix for a two-qubit system constructed from the helicity amplitudes. The formalism is process- and model-independent and classifies the polarization vectors and spin correlations according to their P, CP, and  $C\tilde{P}$  parities. In Section IV, we apply the formalism to construct the

<sup>a</sup>Contact author: sychoi@jbnu.ac.kr

<sup>b</sup>Contact author: dongwookang@jbnu.ac.kr

<sup>c</sup>Contact author: jslee@jnu.ac.kr

<sup>d</sup>Contact author: cbpark@jnu.ac.kr

<sup>e</sup>These authors contributed equally to this work.

<sup>1</sup>The formation of toponium [25–27] could be involved in the analysis of quantum entanglement near the  $t\bar{t}$  production threshold [23, 24].

luminosity-weighted spin density matrix for polarized colliding photons. Through numerical analysis in Section V, we show that the capability of controlling the colliding-photon polarizations at a PLC significantly enhances the observability of quantum entanglement and Bell inequality violation. Section VI contains our conclusions and summary. In Appendix A, we present the 16 polarization coefficients introduced in Section III.

## II. QUANTUM ENTANGLEMENT OF A TWO-QUBIT SYSTEM

The present work examines the bipartite system of a top and anti-top quark pair explicitly. The framework described in this section, however, is applicable to any bipartite system  $S_A \otimes S_B$  of two spin-1/2 particles, where  $S_A$  and  $S_B$  represent the individual spin-1/2 systems. The quantum state of such a system can be represented by the spin density matrix of a two-qubit system:

$$\rho = \frac{1}{4} \left[ \mathbf{1}_2 \otimes \mathbf{1}_2 + \sum_{i=1}^3 B_i^+ (\sigma_i \otimes \mathbf{1}_2) + \sum_{j=1}^3 B_j^- (\mathbf{1}_2 \otimes \sigma_j) + \sum_{i,j=1}^3 C_{ij} (\sigma_i \otimes \sigma_j) \right], \quad (1)$$

where  $\mathbf{1}_2$  is the  $2 \times 2$  identity matrix and  $\sigma_{1,2,3}$  are the three Pauli matrices, defined as

$$\mathbf{1}_2 = \begin{pmatrix} 1 & 0 \\ 0 & 1 \end{pmatrix}; \quad \sigma_1 = \begin{pmatrix} 0 & 1 \\ 1 & 0 \end{pmatrix}, \quad \sigma_2 = \begin{pmatrix} 0 & -i \\ i & 0 \end{pmatrix}, \quad \sigma_3 = \begin{pmatrix} 1 & 0 \\ 0 & -1 \end{pmatrix}. \quad (2)$$

The polarizations of the two particles are represented by the real coefficients obtained by taking the traces

$$B_i^+ = \text{Tr}[\rho(\sigma_i \otimes \mathbf{1}_2)], \quad B_j^- = \text{Tr}[\rho(\mathbf{1}_2 \otimes \sigma_j)], \quad (3)$$

and their spin correlations are given by <sup>2</sup>

$$C_{ij} = \text{Tr}[\rho(\sigma_i \otimes \sigma_j)], \quad (4)$$

where the indices  $i$  and  $j$ , ranging from 1 to 3, refer to the top and anti-top quarks, respectively, in the subsequent concrete analysis. Explicitly, the spin density matrix  $\rho$  in Eq. (1) can be expressed in a  $4 \times 4$  matrix form as

$$\rho = \frac{1}{4} \begin{pmatrix} 1 + B_3^+ + B_3^- + C_{33} & B_1^- + C_{31} - i(B_2^- + C_{32}) & B_1^+ + C_{13} - i(B_2^+ + C_{23}) & C_{11} - C_{22} - i(C_{12} + C_{21}) \\ B_1^- + C_{31} + i(B_2^- + C_{32}) & 1 + B_3^+ - B_3^- - C_{33} & C_{11} + C_{22} + i(C_{12} - C_{21}) & B_1^+ - C_{13} - i(B_2^+ - C_{23}) \\ B_1^+ + C_{13} + i(B_2^+ + C_{23}) & C_{11} + C_{22} + i(C_{21} - C_{12}) & 1 - B_3^+ + B_3^- - C_{33} & B_1^- - C_{31} - i(B_2^- - C_{32}) \\ C_{11} - C_{22} + i(C_{21} + C_{12}) & B_1^+ - C_{13} + i(B_2^+ - C_{23}) & B_1^- - C_{31} + i(B_2^- - C_{32}) & 1 - B_3^+ - B_3^- + C_{33} \end{pmatrix}, \quad (5)$$

in the Hilbert space formed by the orthonormal basis,  $(|++\rangle, |+-\rangle, |-+\rangle, |--\rangle)$ . This explicit form is particularly useful for analyzing the quantum entanglement of the bipartite system.

For a bipartite system of two spin-1/2 particles with spin density matrix  $\rho$ , we adopt the following four established and complementary criteria for quantum entanglement and Bell inequality violation:

- Peres-Horodecki criterion [48]:

$$\rho^{T_B} = (\mathbf{1}_A \otimes T_B)[\rho] < 0 \iff \text{entangled}, \quad (6)$$

where  $T_B$  denotes partial transposition on the subsystem  $S_B$  and the inequality  $\rho^{T_B} < 0$  means that at least one of the four eigenvalues of the partially transposed matrix  $\rho^{T_B}$  is negative. The Peres-Horodecki criterion is comprehensive and thorough. It is applicable not only to two qubits ( $d = d_A = d_B = 2$ ) but also to a qubit-qudit system ( $d_A = 2, d_B = 3$ ). To quantify the Peres-Horodecki criterion, we use the negativity,  $\mathcal{N}[\rho]$ , as an entanglement quantifier, defined as

$$\mathcal{N}[\rho] = \sum_k \frac{|\lambda_k| - \lambda_k}{2} = \sum_{\lambda_k < 0} |\lambda_k|, \quad (7)$$

<sup>2</sup>The following identities hold for tensor products:  $(A \otimes B)(C \otimes D) = AC \otimes BD$  and  $\text{Tr}(A \otimes B) = \text{Tr}(A)\text{Tr}(B)$ .

where  $\lambda_k$  are the eigenvalues of the partially transposed density matrix  $\rho^{TB}$ .

- Concurrence [49]:

$$\mathcal{C}[\rho] = \max(0, r_1 - r_2 - r_3 - r_4) > 0 \iff \text{entangled}, \quad (8)$$

where  $r_{1,2,3,4}$  with  $r_1 \geq r_{2,3,4}$  are the *square roots* of nonnegative eigenvalues of the  $4 \times 4$  auxiliary matrix  $R$  constructed using a two-qubit  $4 \times 4$  density matrix  $\rho$ :

$$R = \rho (\sigma_2 \otimes \sigma_2) \rho^* (\sigma_2 \otimes \sigma_2), \quad (9)$$

which is non-Hermitian but its eigenvalues are always nonnegative.

- Cluser-Horne-Shimony-Holt (CHSH) inequality augmented by the Horodecki condition [50, 51]:

$$m_{12} \equiv m_1 + m_2 > 1 \iff \text{violation of Bell inequality}, \quad (10)$$

where  $m_1 \geq m_2 \geq m_3$  are the three eigenvalues of the following symmetric matrix

$$M = CC^T, \quad (11)$$

with  $C$  being the  $3 \times 3$  spin correlation matrix denoted by  $C_{ij}$  in Eq. (1). Note that the violation of the Bell inequality is a sufficient condition for quantum entanglement.

- Entanglement marker  $D$ :

$$D \equiv \frac{1}{3} \Delta_E < -\frac{1}{3} \implies \text{entangled}, \quad (12)$$

where [2]

$$\Delta_E = C_{11} - |C_{22} + C_{33}|. \quad (13)$$

While this criterion is only a sufficient condition for quantum entanglement derived from the Peres-Horodecki criterion, it provides a practical means of detecting quantum entanglement. When the diagonal components of the  $3 \times 3$  correlation matrix  $C$  are all negative,  $D = \text{Tr}[C]/3$ , which is the observable adopted by the ATLAS and CMS collaborations to probe entanglement near the  $t\bar{t}$  production threshold [4, 5].

### III. SPIN DENSITY MATRIX OF A TWO-QUBIT SYSTEM

The two-photon process  $\gamma\gamma \rightarrow t\bar{t}$  with on-shell top and anti-top quarks receives two tree-level contributions. For the process

$$\gamma(k_1, \lambda_1) + \gamma(k_2, \lambda_2) \rightarrow t(p, \sigma) + \bar{t}(\bar{p}, \bar{\sigma}), \quad (14)$$

where  $\lambda_1$  and  $\lambda_2$  denote the helicities of the colliding photons and  $\sigma$  and  $\bar{\sigma}$  denote the helicities of the top and anti-top quarks, the helicity amplitude in the  $\gamma\gamma$  center-of-mass frame is given by [52]

$$\mathcal{M}_{\lambda_1\lambda_2;\sigma\bar{\sigma}} \equiv \mathcal{A}_C \langle \sigma\bar{\sigma}; \lambda_1\lambda_2 \rangle = \frac{8\pi\alpha Q_t^2}{1 - \beta^2 \cos^2 \Theta} \langle \sigma\bar{\sigma}; \lambda_1\lambda_2 \rangle \quad \text{with} \quad \mathcal{A}_C = \frac{8\pi\alpha Q_t^2}{1 - \beta^2 \cos^2 \Theta}, \quad (15)$$

where  $\lambda_1, \lambda_2, \sigma, \bar{\sigma} = \pm$  are used for notational convenience. Here,  $Q_t = 2/3$ ,  $\beta^2 = 1 - 4M_t^2/\hat{s}$ , and  $\Theta$  is the angle between  $\vec{k}_1$  and  $\vec{p}$  in the production plane, with  $\hat{s} = (k_1 + k_2)^2 = (p + \bar{p})^2$ . The photon backscattered off the incoming  $e^-$  ( $e^+$ ) carries four-momentum  $k_1$  ( $k_2$ ), as illustrated in Fig. 1. The reduced amplitudes  $\langle \sigma\bar{\sigma}; \lambda_1\lambda_2 \rangle$  are given in Table I. Notably, the amplitude vanishes when  $\lambda_1 = \lambda_2$  and  $\sigma = -\bar{\sigma}$  owing to exact cancellations between the  $t$ - and  $u$ -channel diagrams.

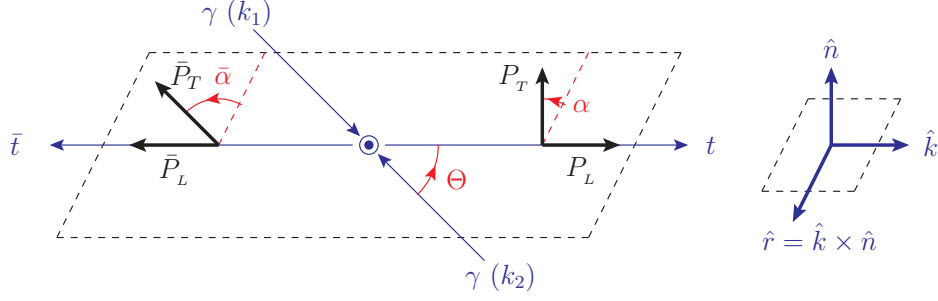


FIG. 1. The  $t\bar{t}$  production plane with the definition of the scattering angle  $\Theta$  for the process  $\gamma(k_1, \lambda_1) + \gamma(k_2, \lambda_2) \rightarrow t(p, \sigma) + \bar{t}(\bar{p}, \bar{\sigma})$ . The four-momentum  $k_1$  ( $k_2$ ) is assigned to the photon backscattered off the incoming  $e^-$  ( $e^+$ ) at the PLC. The transverse polarization vectors  $P_T$  and  $\bar{P}_T$  have azimuthal angles  $\alpha$  and  $\bar{\alpha}$  appearing in Eq. (19), respectively, measured from the production plane. The  $\{\hat{n}, \hat{r}, \hat{k}\}$  basis is defined by  $\hat{k} = \vec{p}/|\vec{p}|$ ,  $\hat{n} = \vec{k}_1 \times \vec{p}/|\vec{k}_1 \times \vec{p}|$ , and  $\hat{r} = \hat{k} \times \hat{n}$ . Note that, in the  $\{\hat{n}, \hat{r}, \hat{k}\}$  basis,  $P_L = P_k$ ,  $P_{T\alpha} = -P_r$ , and  $P_{T\alpha} = P_n$  for the top quark, whereas for the anti-top quark,  $\bar{P}_L = -\bar{P}_k$ ,  $\bar{P}_{T\bar{\alpha}} = -\bar{P}_r$ , and  $\bar{P}_{T\bar{\alpha}} = \bar{P}_n$ .

TABLE I. The reduced amplitudes  $\langle \sigma\bar{\sigma}; \lambda_1\lambda_2 \rangle$  in Eq. (15). Here,  $\beta = \sqrt{1 - 4M_t^2/\hat{s}}$ , where  $M_t$  denotes the pole mass of the top quark, and  $\Theta$  is the angle between  $\vec{k}_1$  and  $\vec{p}$  in the production plane (see Fig. 1).

$(\lambda_1\lambda_2) \downarrow (\sigma\bar{\sigma}) \rightarrow$	$\langle ++ \rangle$	$\langle -- \rangle$	$\langle -+ \rangle$	$\langle +- \rangle$
$\langle ++ \rangle$	$\frac{2M_t}{\sqrt{\hat{s}}} [1 + \beta]$	$\frac{2M_t}{\sqrt{\hat{s}}} [1 - \beta]$	0	0
$\langle -- \rangle$	$\frac{2M_t}{\sqrt{\hat{s}}} [-1 + \beta]$	$\frac{2M_t}{\sqrt{\hat{s}}} [-1 - \beta]$	0	0
$\langle -+ \rangle$	$-\frac{2M_t}{\sqrt{\hat{s}}} \beta \sin^2 \Theta$	$\frac{2M_t}{\sqrt{\hat{s}}} \beta \sin^2 \Theta$	$-\beta \sin \Theta (\cos \Theta + 1)$	$-\beta \sin \Theta (\cos \Theta - 1)$
$\langle +- \rangle$	$-\frac{2M_t}{\sqrt{\hat{s}}} \beta \sin^2 \Theta$	$\frac{2M_t}{\sqrt{\hat{s}}} \beta \sin^2 \Theta$	$-\beta \sin \Theta (\cos \Theta - 1)$	$-\beta \sin \Theta (\cos \Theta + 1)$

Note that the reduced amplitudes transform under P, CP, and  $\text{CPT}$  as follows:

$$\begin{aligned}
\langle \sigma\bar{\sigma}; \lambda_1, \lambda_2 \rangle &\xleftarrow{\text{P}} -(-1)^{(\sigma-\bar{\sigma})/2} \langle -\sigma, -\bar{\sigma}; -\lambda_1, -\lambda_2 \rangle; \\
\langle \sigma\bar{\sigma}; \lambda_1, \lambda_2 \rangle &\xleftarrow{\text{CP}} -(-1)^{(\sigma-\bar{\sigma})/2} \langle -\bar{\sigma}, -\sigma; -\lambda_2, -\lambda_1 \rangle; \\
\langle \sigma\bar{\sigma}; \lambda_1, \lambda_2 \rangle &\xleftarrow{\text{CPT}} -(-1)^{(\sigma-\bar{\sigma})/2} \langle -\bar{\sigma}, -\sigma; -\lambda_2, -\lambda_1 \rangle^*,
\end{aligned} \tag{16}$$

or equivalently,

$$\begin{aligned}
\langle \pm\pm; \lambda_1, \lambda_2 \rangle &\xleftarrow{\text{P}} -\langle \mp\mp; -\lambda_1, -\lambda_2 \rangle, & \langle \pm\mp; \lambda_1, \lambda_2 \rangle &\xleftarrow{\text{P}} \langle \mp\pm; -\lambda_1, -\lambda_2 \rangle; \\
\langle \pm\pm; \lambda_1, \lambda_2 \rangle &\xleftarrow{\text{CP}} -\langle \mp\mp; -\lambda_2, -\lambda_1 \rangle, & \langle \pm\mp; \lambda_1, \lambda_2 \rangle &\xleftarrow{\text{CP}} \langle \mp\mp; -\lambda_2, -\lambda_1 \rangle; \\
\langle \pm\pm; \lambda_1, \lambda_2 \rangle &\xleftarrow{\text{CPT}} -\langle \mp\mp; -\lambda_2, -\lambda_1 \rangle^*, & \langle \pm\mp; \lambda_1, \lambda_2 \rangle &\xleftarrow{\text{CPT}} \langle \mp\mp; -\lambda_2, -\lambda_1 \rangle^*.
\end{aligned} \tag{17}$$

As a result of these transformation properties of the helicity amplitudes, each polarization coefficient possesses definite P, CP, and  $\text{CPT}$  parities, as will be shown shortly.

To streamline the analysis of the  $t\bar{t}$  spin correlations, we arrange the helicity amplitudes in Eq. (15) into a  $2 \times 2$  matrix:

$$\mathcal{M} = \mathcal{A}_C \begin{pmatrix} \langle ++; \lambda_1\lambda_2 \rangle & \langle +-; \lambda_1\lambda_2 \rangle \\ \langle -+; \lambda_1\lambda_2 \rangle & \langle --; \lambda_1\lambda_2 \rangle \end{pmatrix} \equiv \mathcal{A}_C \mathbf{M}. \tag{18}$$

Contracting the matrix  $\mathcal{M}$  and its Hermitian conjugate  $\mathcal{M}^\dagger$  with the  $2 \times 2$  spin density matrices for the top and anti-top quarks, defined as

$$\rho_t = \frac{1}{2} \begin{pmatrix} 1 + P_L & P_T e^{-i\alpha} \\ P_T e^{i\alpha} & 1 - P_L \end{pmatrix}, \quad \bar{\rho}_t = \frac{1}{2} \begin{pmatrix} 1 + \bar{P}_L & -\bar{P}_T e^{i\bar{\alpha}} \\ -\bar{P}_T e^{-i\bar{\alpha}} & 1 - \bar{P}_L \end{pmatrix}, \quad (19)$$

we obtain the polarization-weighted amplitude squared given by [53]

$$\overline{|\mathcal{M}|^2} = \frac{1}{4} \sum_{\lambda_1, \lambda_2 = \pm} \text{Tr} [\mathcal{M} \bar{\rho}_t^T \mathcal{M}^\dagger \rho_t] = \frac{1}{4} |\mathcal{A}_C|^2 \sum_{\lambda_1, \lambda_2 = \pm} \text{Tr} [\mathbf{M} \bar{\rho}_t^T \mathbf{M}^\dagger \rho_t] \equiv \frac{1}{4} |\mathcal{A}_C|^2 \widehat{\Sigma}. \quad (20)$$

By identifying  $P_L = P_k$ ,  $P_T c_\alpha = -P_r$ , and  $P_T s_\alpha = P_n$  for the top quark and  $\bar{P}_L = -\bar{P}_k$ ,  $\bar{P}_T c_{\bar{\alpha}} = -\bar{P}_r$  and  $\bar{P}_T s_{\bar{\alpha}} = \bar{P}_n$  for the anti-top quark in the  $\{\hat{n}, \hat{r}, \hat{k}\}$  basis, see Fig. 1, and evaluating  $\text{Tr} [\mathbf{M} \bar{\rho}_t^T \mathbf{M}^\dagger \rho_t]$  explicitly, we can obtain  $\widehat{\Sigma}$  in terms of the 16 polarization coefficients from  $\widehat{C}_1$  to  $\widehat{C}_{16}$  as follows:

$$\begin{aligned} \widehat{\Sigma} = & (\widehat{C}_1[+++]) + \widehat{C}_3[+++]) \\ & + P_n(\widehat{C}_6[+-] + \widehat{C}_8[+-]) + P_r(-\widehat{C}_5[-++] - \widehat{C}_7[-+-]) + P_k(\widehat{C}_2[-+-] + \widehat{C}_4[-+-]) \\ & + \bar{P}_n(\widehat{C}_6[+-] - \widehat{C}_8[+-]) + \bar{P}_r(-\widehat{C}_5[-++] + \widehat{C}_7[-+-]) + \bar{P}_k(-\widehat{C}_2[-+-] + \widehat{C}_4[-+-]) \\ & + P_n \bar{P}_n(\widehat{C}_{13}[+++]) - \widehat{C}_{15}[+++]) + P_n \bar{P}_r(-\widehat{C}_{14}[-+-] - \widehat{C}_{16}[-+-]) + P_n \bar{P}_k(-\widehat{C}_{10}[-+-] - \widehat{C}_{12}[-+-]) \\ & + P_r \bar{P}_n(\widehat{C}_{14}[-+-] - \widehat{C}_{16}[-+-]) + P_r \bar{P}_r(\widehat{C}_{13}[+++]) + \widehat{C}_{15}[+++]) + P_r \bar{P}_k(\widehat{C}_9[+-] + \widehat{C}_{11}[+-]) \\ & + P_k \bar{P}_n(\widehat{C}_{10}[-+-] - \widehat{C}_{12}[-+-]) + P_k \bar{P}_r(-\widehat{C}_9[+-] + \widehat{C}_{11}[+-]) + P_k \bar{P}_k(-\widehat{C}_1[+++]) + \widehat{C}_3[+++]), \quad (21) \end{aligned}$$

where the P, CP, and CPT parities of each polarization coefficient, derived from the transformation rules of the reduced amplitudes given in Eq. (16), are denoted in square brackets. The explicit forms of all 16 polarization coefficients in terms of the reduced amplitudes are given in Appendix A. Our classification and parity assignments are in excellent agreement with those reported in Ref. [54].

TABLE II. The P, CP, and CPT parities of the 16 polarization coefficients and their related physical quantities.

Polarization coefficient	$\widehat{C}_1$	$\widehat{C}_2$	$\widehat{C}_3$	$\widehat{C}_4$	$\widehat{C}_5$	$\widehat{C}_6$	$\widehat{C}_7$	$\widehat{C}_8$
[P, CP, CPT] Parities	[+++]	[- - -]	[+++]	[- + +]	[- + +]	[+ + -]	[- - -]	[+ - +]
Physical quantity	$\frac{\widehat{A} - \widehat{C}_{kk}}{2}$	$\frac{\widehat{B}_k^+ - \widehat{B}_k^-}{2}$	$\frac{\widehat{A} + \widehat{C}_{kk}}{2}$	$\frac{\widehat{B}_k^+ + \widehat{B}_k^-}{2}$	$-\frac{\widehat{B}_r^+ + \widehat{B}_r^-}{2}$	$\frac{\widehat{B}_n^+ + \widehat{B}_n^-}{2}$	$-\frac{\widehat{B}_r^+ - \widehat{B}_r^-}{2}$	$\frac{\widehat{B}_n^+ - \widehat{B}_n^-}{2}$
Polarization coefficient	$\widehat{C}_9$	$\widehat{C}_{10}$	$\widehat{C}_{11}$	$\widehat{C}_{12}$	$\widehat{C}_{13}$	$\widehat{C}_{14}$	$\widehat{C}_{15}$	$\widehat{C}_{16}$
[P, CP, CPT] Parities	[+ - -]	[- - +]	[+++]	[- + -]	[+++]	[- - +]	[+++]	[- + -]
Physical quantity	$\frac{\widehat{C}_{rk} - \widehat{C}_{kr}}{2}$	$\frac{\widehat{C}_{kn} - \widehat{C}_{nk}}{2}$	$\frac{\widehat{C}_{rk} + \widehat{C}_{kr}}{2}$	$-\frac{\widehat{C}_{kn} + \widehat{C}_{nk}}{2}$	$\frac{\widehat{C}_{nn} + \widehat{C}_{rr}}{2}$	$\frac{\widehat{C}_{rn} - \widehat{C}_{nr}}{2}$	$\frac{\widehat{C}_{rr} - \widehat{C}_{nn}}{2}$	$-\frac{\widehat{C}_{rn} + \widehat{C}_{nr}}{2}$

Table II lists the P, CP, and CPT parities of the 16 polarization coefficients and the related physical observables extractable from  $t\bar{t}$  production and the angular distributions of their decay products. At leading order (LO) in QED, only the [+++] parity coefficients  $\widehat{C}_1$ ,  $\widehat{C}_3$ ,  $\widehat{C}_{11}$ ,  $\widehat{C}_{13}$ , and  $\widehat{C}_{15}$  are nonzero. Consequently, all polarization vectors  $\widehat{B}_i^+$  and  $\widehat{B}_j^-$  vanish. The spin correlation matrix is then simplified, with only the elements  $\widehat{C}_{nn}$ ,  $\widehat{C}_{rr}$ ,  $\widehat{C}_{kk}$ ,  $\widehat{C}_{rk}$ , and  $\widehat{C}_{kr}$  remaining. Since  $\widehat{C}_9$  (with [+ - -] parity) vanishes at LO, we further have  $\widehat{C}_{rk} = \widehat{C}_{kr}$ .

While the preceding simplification holds at LO in QED, it breaks down beyond LO, even within the Standard Model (SM) [54]. Electroweak and QCD quantum corrections, incorporating P and CP violation in the electroweak sector, generate absorptive parts and introduce P, CP, and CPT-violating effects. This implies that all 16 polarization coefficients

can potentially contribute beyond LO and/or beyond the SM. Importantly, our amplitude-based formalism for constructing the spin density matrix of a two-qubit system offers a crucial advantage. Its process- and model-independent structure, combined with its ability to classify physical observables by their P, CP, and  $\text{CPT}$  parities, makes it a powerful probe for pinpointing new-physics contributions beyond the SM, even in the presence of these complex corrections.

The final form of  $\hat{\Sigma}$  in Eq. (21) leads to the spin density matrix in the  $\{\hat{n}, \hat{r}, \hat{k}\}$  basis,

$$\rho = \frac{1}{4} \left[ \mathbf{1}_2 \otimes \mathbf{1}_2 + \frac{1}{\hat{A}} \sum_{i=n,r,k} \hat{B}_i^+ (\sigma_i \otimes \mathbf{1}_2) + \frac{1}{\hat{A}} \sum_{j=n,r,k} \hat{B}_j^- (\mathbf{1}_2 \otimes \sigma_j) + \frac{1}{\hat{A}} \sum_{i,j=n,r,k} \hat{C}_{ij} (\sigma_i \otimes \sigma_j) \right], \quad (22)$$

where the *unnormalized* polarization vectors  $\hat{B}_i^+$  and  $\hat{B}_j^-$  for the top and anti-top quarks are given by

$$\begin{aligned} \hat{B}_i^+ &= (\hat{C}_6[+-] + \hat{C}_8[+-], -\hat{C}_5[-++] - \hat{C}_7[---], \hat{C}_2[---] + \hat{C}_4[-++]), \\ \hat{B}_j^- &= (\hat{C}_6[+-] - \hat{C}_8[+-], -\hat{C}_5[-++] + \hat{C}_7[---], -\hat{C}_2[---] + \hat{C}_4[-++]), \end{aligned} \quad (23)$$

respectively, and the *unnormalized*  $3 \times 3$  spin correlation matrix  $\hat{C}_{ij}$  by

$$\hat{C}_{ij} = \begin{pmatrix} \hat{C}_{13}[+++]-\hat{C}_{15}[+++] & -\hat{C}_{14}[-++] - \hat{C}_{16}[-+-] & -\hat{C}_{10}[-+-] - \hat{C}_{12}[-+-] \\ \hat{C}_{14}[-++] - \hat{C}_{16}[-+-] & \hat{C}_{13}[+++] + \hat{C}_{15}[+++] & \hat{C}_9[+-] + \hat{C}_{11}[+++] \\ \hat{C}_{10}[-+-] - \hat{C}_{12}[-+-] & -\hat{C}_9[+-] + \hat{C}_{11}[+++] & -\hat{C}_1[+++] + \hat{C}_3[+++] \end{pmatrix}. \quad (24)$$

On the other hand, the normalization factor, defined by

$$\hat{A} = \hat{C}_1[+++] + \hat{C}_3[+++], \quad (25)$$

is related to the unpolarized differential cross section. The explicit form of this relationship is

$$d\hat{\sigma}_0 = \frac{1}{2\hat{s}} N_c \overline{|\mathcal{M}|^2} d\Phi_2 = \frac{1}{2\hat{s}} N_c \left[ \frac{|\mathcal{A}_C|^2}{4} \sum_{\lambda_1, \lambda_2, \sigma, \bar{\sigma}} |(\sigma \bar{\sigma}; \lambda_1 \lambda_2)|^2 \right] \frac{\beta}{16\pi} d\cos\Theta = \frac{\beta N_c}{32\pi\hat{s}} |\mathcal{A}_C|^2 \hat{A} d\cos\Theta, \quad (26)$$

with the color factor  $N_c = 3$  in the SM.

In summary, we have developed an amplitude-level formalism for constructing the spin density matrix of a two-qubit system. While the present analysis focuses on the specific SM process  $\gamma\gamma \rightarrow t\bar{t}$  at a PLC, the formalism itself is not restricted to this particular example. Its process- and model-independent structure provides a systematic framework for classifying the polarization vectors and spin correlations of the spin density matrix according to their fundamental P, CP, and  $\text{CPT}$  parities, making it applicable to a wide range of processes and models beyond the SM.

#### IV. LUMINOSITY-WEIGHTED SPIN DENSITY MATRIX

A key advantage of PLCs is the efficient control of colliding photon helicities through careful optimization of the initial electron and positron beam polarizations and the laser beams used in the Compton backscattering process [40–42]. Beyond this efficient polarization control, specific polarization configurations offer the remarkable possibility of significantly enhancing the  $\gamma\gamma$  luminosity within narrow regions of  $\sqrt{\hat{s}}$ . These regions are of particular interest, as they may maximize quantum entanglement and/or enable observation of Bell inequality violation. The electron and positron beam polarizations are denoted  $P_e$  and  $\tilde{P}_e$ , respectively; the degrees of circular polarization of the initial laser photons are denoted  $P_c$  and  $\tilde{P}_c$ . Specifically, the combinations  $P_e P_c = \tilde{P}_e \tilde{P}_c = -1$ , chosen for our numerical analysis in the next section, exhibit such enhanced luminosity. For this reason, transverse polarizations of the laser beams are not considered in the present study. In this section, we demonstrate how a PLC can be used to achieve these enhanced capabilities.

We begin by defining the machine parameter  $x$ , which depends on the beam energy  $E_b = \sqrt{s}/2$  and the laser-photon energy  $\omega_0$ :

$$x = \frac{4E_b\omega_0}{M_e^2} = 15.3 \left( \frac{E_b}{\text{TeV}} \right) \left( \frac{\omega_0}{\text{eV}} \right), \quad (27)$$

where  $s = (p_{e^-} + p_{e^+})^2$  is the center-of-mass energy squared of the initial  $e^+e^-$  pair. The  $\gamma\gamma$  luminosity of the two colliding photons with the helicity combination of  $(\lambda_1, \lambda_2)$  reads

$$\frac{1}{\mathcal{L}_{ee}} \frac{d\mathcal{L}_{\gamma\gamma}^{\lambda_1\lambda_2}}{d\tau} = \left( \langle 00 \rangle_\tau + \lambda_1 \langle 20 \rangle_\tau + \lambda_2 \langle 02 \rangle_\tau + \lambda_1 \lambda_2 \langle 22 \rangle_\tau \right) \left( \frac{2\pi\alpha^2}{\sigma_c^{\gamma_1} x M_e^2} \right) \left( \frac{2\pi\alpha^2}{\sigma_c^{\gamma_2} x M_e^2} \right), \quad (28)$$

with  $\tau = \hat{s}/s$ . The total cross sections for the two Compton scattering processes, denoted by  $\sigma_c^{\gamma_1}$  and  $\sigma_c^{\gamma_2}$ , are given by

$$\sigma_c^{\gamma_1} = \sigma_c^0 + P_e P_c \sigma_c^1; \quad \sigma_c^{\gamma_2} = \sigma_c^0 + \tilde{P}_e \tilde{P}_c \sigma_c^1. \quad (29)$$

The cross sections  $\sigma_c^0$  and  $\sigma_c^1$  depend on the machine parameter  $x$  as

$$\begin{aligned} \sigma_c^0 &= \frac{2\pi\alpha^2}{x M_e^2} \left[ \left( 1 - \frac{4}{x} - \frac{8}{x^2} \right) \log(x+1) + \frac{1}{2} + \frac{8}{x} - \frac{1}{2(x+1)^2} \right], \\ \sigma_c^1 &= \frac{2\pi\alpha^2}{x M_e^2} \left[ \left( 1 + \frac{2}{x} \right) \log(x+1) - \frac{5}{2} + \frac{1}{x+1} - \frac{1}{2(x+1)^2} \right]. \end{aligned} \quad (30)$$

The polarization correlation functions appearing in Eq. (28) are defined through a convolution integral, given by

$$\langle ij \rangle_\tau \equiv \int_{\tau/y_{\max}}^{y_{\max}} \frac{dy}{y} f_i(y) \tilde{f}_j(\tau/y), \quad (31)$$

with  $i, j = 0, 2$ , where  $y_{\max} = x/(1+x)$ . The functions within the integrals are

$$\begin{aligned} f_0(y) &= \frac{1}{1-y} + (1-y) - 4r(1-r) - rx(2r-1)(2-y)P_e P_c, \\ f_2(y) &= rx \left[ 1 + (1-y)(2r-1)^2 \right] P_e - (2r-1) \left( \frac{1}{1-y} + 1-y \right) P_c; \\ \tilde{f}_0(\tau/y) &= \frac{1}{1-\tau/y} + (1-\tau/y) - 4\tilde{r}(1-\tilde{r}) - \tilde{r}x(2\tilde{r}-1)(2-\tau/y)\tilde{P}_e \tilde{P}_c, \\ \tilde{f}_2(\tau/y) &= \tilde{r}x \left[ 1 + (1-\tau/y)(2\tilde{r}-1)^2 \right] \tilde{P}_e - (2\tilde{r}-1) \left( \frac{1}{1-\tau/y} + 1-\tau/y \right) \tilde{P}_c, \end{aligned} \quad (32)$$

where  $y$  is the fraction of the  $e^-$  energy transferred to the photon, and

$$r = \frac{y}{x(1-y)}, \quad \tilde{r} = \frac{\tau/y}{x(1-\tau/y)}. \quad (33)$$

For the unpolarized case  $P_e = P_c = \tilde{P}_e = \tilde{P}_c = 0$ , only the correlation function  $\langle 00 \rangle_\tau$  is nonvanishing, resulting in the following helicity-independent unpolarized luminosity:

$$\frac{1}{\mathcal{L}_{ee}} \frac{d\mathcal{L}_{\gamma\gamma}^{\lambda_1\lambda_2}}{d\tau} \Big|_{P_e=P_c=\tilde{P}_e=\tilde{P}_c=0} = \langle 00 \rangle_\tau^{\text{unp}} \left( \frac{2\pi\alpha^2}{\sigma_c^{\gamma_1} x M_e^2} \right) \left( \frac{2\pi\alpha^2}{\sigma_c^{\gamma_2} x M_e^2} \right) \equiv \frac{1}{\mathcal{L}_{ee}} \frac{d\mathcal{L}_{\gamma\gamma}^{\text{unp}}}{d\tau}, \quad (34)$$

where  $\langle 00 \rangle_\tau^{\text{unp}}$  represents the polarization correlation function  $\langle 00 \rangle_\tau$  evaluated in the unpolarized case, where  $P_e P_c = \tilde{P}_e \tilde{P}_c = 0$ . The differential unpolarized cross section is then found to be:

$$\frac{1}{\mathcal{L}_{ee}} \frac{d^2\hat{\sigma}_0}{d\tau d\cos\Theta} = \frac{1}{\mathcal{L}_{ee}} \frac{d\mathcal{L}_{\gamma\gamma}^{\text{unp}}}{d\tau} \frac{d\hat{\sigma}_0}{d\cos\Theta} = \frac{\beta N_c}{32\pi\hat{s}} |\mathcal{A}_C|^2 \left[ \frac{1}{\mathcal{L}_{ee}} \frac{d\mathcal{L}_{\gamma\gamma}^{\text{unp}}}{d\tau} \left( \hat{C}_1 + \hat{C}_3 \right) \right], \quad (35)$$

with the color factor  $N_c = 3$ .

To obtain the spin density matrix taking account of the helicity-dependent  $\gamma\gamma$  luminosity (28), we first note that one can decompose each coefficient  $\hat{C}_i$  into a sum over photon helicities as

$$\hat{C}_i = \sum_{\lambda_1, \lambda_2 = \pm} c_i^{\lambda_1\lambda_2}, \quad (36)$$

and introduce the luminosity-weighted polarization coefficients  $\widehat{C}_i^w$ , which are defined as

$$\widehat{C}_i^w \equiv \sum_{\lambda_1, \lambda_2 = \pm} w^{\lambda_1 \lambda_2} c_i^{\lambda_1 \lambda_2}, \quad (37)$$

where the weight functions are defined by

$$w^{\lambda_1 \lambda_2} \equiv \frac{L^{\lambda_1 \lambda_2}}{\sum_{\lambda_1, \lambda_2 = \pm} L^{\lambda_1 \lambda_2}}, \quad (38)$$

with the luminosity functions

$$L^{\lambda_1 \lambda_2} \equiv \frac{1}{\mathcal{L}_{ee}} \frac{d\mathcal{L}_{\gamma\gamma}^{\lambda_1 \lambda_2}}{d\sqrt{\tau}}. \quad (39)$$

The average of the helicity-dependent  $\gamma\gamma$  luminosities is determined solely by  $\langle 00 \rangle_\tau$ , as can be checked from Eq. (28). This correlation is, in turn, a function depending only on the products  $P_e P_c$  and  $\tilde{P}_e \tilde{P}_c$ , as evident in Eq. (32). When  $P_e = P_c = \tilde{P}_e = \tilde{P}_c = 0$ , the average reduces to the unpolarized luminosity given by Eq. (34):

$$\frac{1}{4} \sum_{\lambda_1, \lambda_2 = \pm} L^{\lambda_1 \lambda_2} = \frac{1}{4} \sum_{\lambda_1, \lambda_2 = \pm} \frac{1}{\mathcal{L}_{ee}} \frac{d\mathcal{L}_{\gamma\gamma}^{\lambda_1 \lambda_2}}{d\sqrt{\tau}} \xrightarrow{P_e P_c = \tilde{P}_e \tilde{P}_c = 0} \frac{1}{\mathcal{L}_{ee}} \frac{d\mathcal{L}_{\gamma\gamma}^{\text{unp}}}{d\sqrt{\tau}}. \quad (40)$$

Collecting the above results, the luminosity-weighted spin density matrix retains the form of Eq. (22), with the sole effect of luminosity weighting being the replacement of each unweighted coefficient  $\widehat{C}_i$  by its luminosity-weighted counterpart  $\widehat{C}_i^w$  in the polarization vectors, spin correlations, and normalization factor defined in Eqs. (23), (24), and (25).

The helicity-dependent luminosities  $L^{\lambda_1 \lambda_2}$  defined in Eq. (39) are plotted in the left panel of Fig. 2 for the specific polarization configuration  $P_e P_c = \tilde{P}_e \tilde{P}_c = -1$ , with the machine parameter set to  $x = 4.8$ . The frames of the  $4 \times 4$  grid are arranged with the colliding photon polarizations  $(\lambda_1, \lambda_2) = (+, +), (-, -), (-, +), (+, -)$  displayed from left to

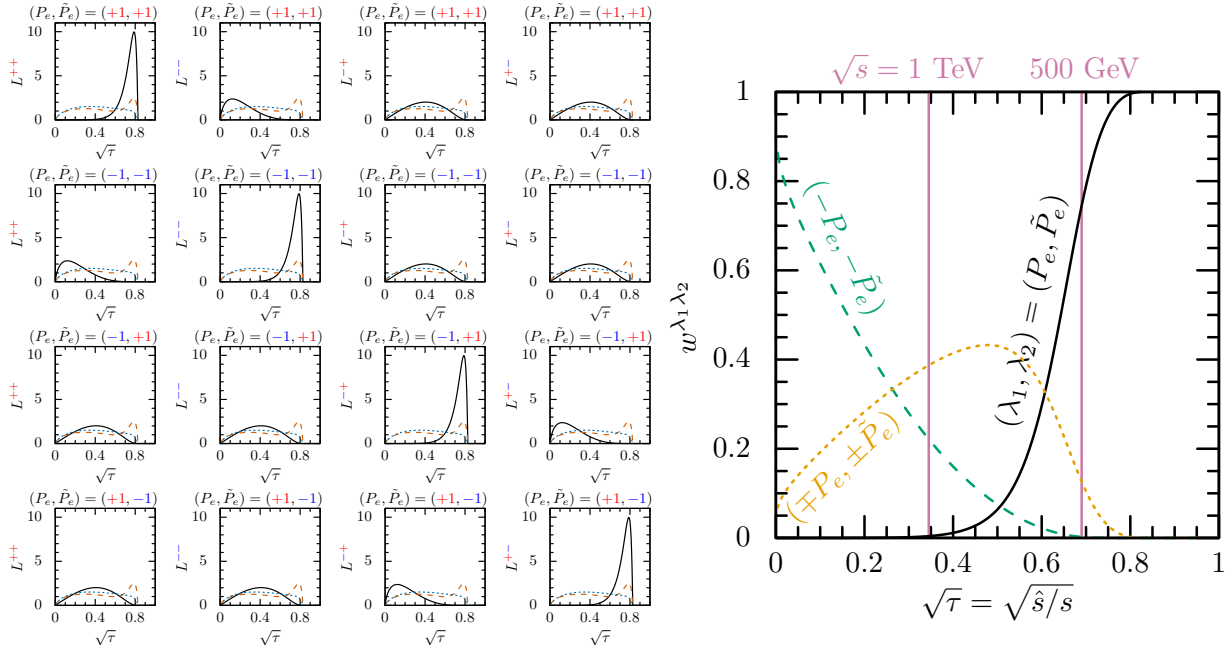


FIG. 2. (Left) The helicity-dependent luminosities  $L^{\lambda_1 \lambda_2} = \frac{1}{\mathcal{L}_{ee}} \frac{d\mathcal{L}_{\gamma\gamma}^{\lambda_1 \lambda_2}}{d\sqrt{\tau}}$  taking  $P_e P_c = \tilde{P}_e \tilde{P}_c = -1$  and  $x = 4.8$ . From left to right,  $(\lambda_1, \lambda_2) = (+, +), (-, -), (-, +)$ , and  $(+, -)$  while, from top to bottom,  $(P_e = -P_c, \tilde{P}_e = -\tilde{P}_c) = (+, +), (-, -), (-, +)$ , and  $(+, -)$ . In each frame, we also show the average luminosity  $\frac{1}{4} \sum_{\lambda_1, \lambda_2 = \pm} L^{\lambda_1 \lambda_2}$  and the unpolarized one  $\frac{1}{\mathcal{L}_{ee}} \frac{d\mathcal{L}_{\gamma\gamma}^{\text{unp}}}{d\sqrt{\tau}}$  in dashed red and blue lines, respectively, for comparison. (Right) The weight functions  $w^{\lambda_1 \lambda_2}$  for  $(\lambda_1, \lambda_2) = (P_e, \tilde{P}_e)$  (black solid),  $(\lambda_1, \lambda_2) = (-P_e, -\tilde{P}_e)$  (green dashed), and  $(\lambda_1, \lambda_2) = (\mp P_e, \pm \tilde{P}_e)$  (orange dotted). The vertical lines at  $\sqrt{\tau} = 0.345$  and  $0.69$  mark the  $2M_t$  threshold for  $\sqrt{s} = 1$  TeV and 500 GeV, respectively.

right, and the initial electron and positron polarizations  $(P_e, \tilde{P}_e) = (+, +), (-, -), (-, +), (+, -)$  displayed from top to bottom.<sup>3</sup> The initial laser beam polarizations,  $P_c$  and  $\tilde{P}_c$ , are fixed by the condition  $P_e P_c = \tilde{P}_e \tilde{P}_c = -1$ . For comparison, each frame also displays the helicity-independent average luminosity,  $\sum_{\lambda_1, \lambda_2 = \pm} L^{\lambda_1 \lambda_2} / 4$ , and the unpolarized luminosity,  $\frac{1}{\mathcal{L}_{ee}} \frac{d\mathcal{L}_{\gamma\gamma}^{\text{unp}}}{d\sqrt{\tau}}$ .

We observe that the luminosity functions exhibit pronounced peaks near  $\sqrt{\tau} \simeq 0.8$  when the photon helicities are  $(\lambda_1, \lambda_2) = (P_e, \tilde{P}_e)$ . This behavior clearly demonstrates that a PLC can effectively control the polarization states of colliding photons. Under the condition  $P_e P_c = \tilde{P}_e \tilde{P}_c = -1$ , we find that more than 70% of the colliding photons carry the helicities of the initial electron and positron beams within the kinematic region  $0.68 \lesssim \sqrt{\tau} \lesssim 0.82$  (see the right panel of Fig. 2).<sup>4</sup> For the center-of-mass energy of  $\sqrt{s} = 500$  (1000) GeV, this interval corresponds to invariant masses of  $340$  (680)  $\lesssim \sqrt{\hat{s}}/\text{GeV} \lesssim 410$  (820), spanning energies near (well above) the  $t\bar{t}$  threshold  $2M_t$ . The weight functions for  $(\lambda_1, \lambda_2) = (-P_e, +\tilde{P}_e)$  and  $(\lambda_1, \lambda_2) = (+P_e, -\tilde{P}_e)$  are identical under  $\tilde{P}_e \leftrightarrow -\tilde{P}_e, P_e \leftrightarrow -P_e$ .

## V. NUMERICAL ANALYSIS

Given the spin density matrix in Eq. (1), the four criteria for quantum entanglement and violation of the Bell inequality, as defined in Eqs. (6), (8), (10), and (12), can be readily evaluated. For our numerical analysis of the unpolarized case ( $P_e = P_c = \tilde{P}_e = \tilde{P}_c = 0$ ), we utilize the spin density matrix in Eq. (22), in conjunction with Eqs. (23), (24), and (25). These expressions are formulated using the 16 polarization coefficients  $\hat{C}_i$  detailed in Appendix A in terms of the reduced amplitudes defined in Eq. (15). The LO reduced amplitudes for the  $\gamma\gamma \rightarrow t\bar{t}$  process are provided in Table I. For the analysis of polarized colliding photons, we introduce the luminosity-weighted polarization coefficients  $\hat{C}_i^w$ , as defined in Eq. (37). The luminosity-weighted spin density matrix retains the form of Eq. (22), but with  $\hat{C}_i$  replaced by  $\hat{C}_i^w$  in Eqs. (23), (24), and (25).

This section presents a numerical analysis of the impact of colliding-photon polarization on the observability of quantum entanglement and Bell inequality violation in top-quark pair production at a PLC. After studying the unpolarized case

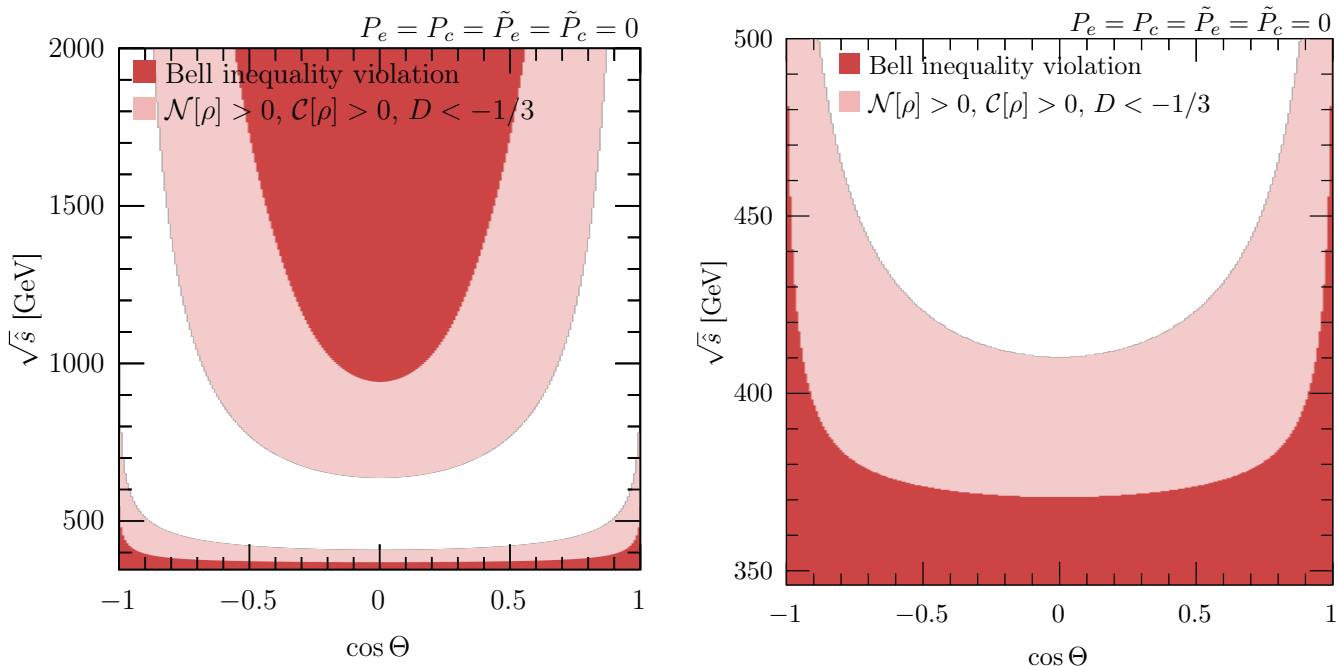


FIG. 3. **Quantum entanglement in the unpolarized case:** (Left) Quantum entanglement for the unpolarized case  $P_e = P_c = \tilde{P}_e = \tilde{P}_c = 0$ , shown in the  $(\cos \Theta, \sqrt{\hat{s}})$  plane. Shaded regions satisfy  $\mathcal{N}[\rho] > 0$ ,  $\mathcal{C}[\rho] > 0$ , and  $D < -1/3$ , indicating entanglement of the  $t\bar{t}$  spin state. The densely shaded red regions additionally satisfy  $m_{12} > 1$ , indicating violation of the Bell inequality. (Right) Magnified view of the region  $2M_t < \sqrt{\hat{s}} < 500$  GeV.

<sup>3</sup>It is understood that, for example,  $(P_e, \tilde{P}_e) = (+, +) = (+1, +1)$  under the condition  $P_e P_c = \tilde{P}_e \tilde{P}_c = -1$ .

<sup>4</sup>More precisely, for  $\lambda_1 = P_e$  and  $\lambda_2 = \tilde{P}_e$ , the weight function satisfies  $w^{\lambda_1 \lambda_2} > 0.7$  (0.9) in the region  $0.68$  (0.73)  $\lesssim \sqrt{\tau} \lesssim 0.82$ .

( $P_e = P_c = \tilde{P}_e = \tilde{P}_c = 0$ ) for comparison, we first examine scenarios with perfectly polarized photons, where only one of the four weight functions  $w^{\lambda_1\lambda_2}$  is nonzero (equal to 1), while the others vanish. Subsequently, to address realistic cases with imperfectly polarized colliding photons containing mixed polarization states, we perform detailed numerical studies for two specific cases:  $\sqrt{s} = 500$  GeV with  $P_e = -P_c = \tilde{P}_e = -\tilde{P}_c = +1$ , and  $\sqrt{s} = 1$  TeV with  $P_e = -P_c = -\tilde{P}_e = +\tilde{P}_c = +1$ .

### A. Unpolarized colliding photons

Figure 3 shows the entanglement region in the  $(\cos\Theta, \sqrt{\hat{s}})$  plane for the unpolarized case ( $P_e = P_c = \tilde{P}_e = \tilde{P}_c = 0$ ). Shaded regions satisfy  $\mathcal{N}[\rho] > 0$ ,  $\mathcal{C}[\rho] > 0$ , and  $D < -1/3$ ; densely shaded red regions additionally satisfy  $m_{12} > 1$ , indicating violation of the Bell inequality. As expected, the criteria  $\mathcal{N}[\rho] > 0$  and  $\mathcal{C}[\rho] > 0$  identify the same regions, and the condition  $D < -1/3$  is equally effective at detecting entanglement. The Bell inequality is violated near the  $2M_t$  threshold and in the region where  $\sqrt{\hat{s}} \gtrsim 1$  TeV and  $|\cos\Theta| \lesssim 0.5$ .

### B. Perfectly polarized colliding photons with $w^{\pm\pm} = 1$

To analyze the scenario with perfectly polarized colliding photons of the same helicity, we first consider the case where  $w^{++} = 1$  and, accordingly,  $w^{--} = w^{+-} = w^{-+} = 0$ . In this configuration with  $\lambda_1 = \lambda_2 = +$ , the luminosity-weighted polarization coefficients  $\hat{C}_i^w$  receive contributions only from the two reduced amplitudes with  $\sigma\bar{\sigma} = \pm\pm$  (see Table I):

$$\langle ++; ++ \rangle = \frac{2M_t}{\sqrt{\hat{s}}}(1 + \beta), \quad \langle --; ++ \rangle = \frac{2M_t}{\sqrt{\hat{s}}}(1 - \beta). \quad (41)$$

Using the explicit expressions for the polarization coefficients in Appendix A, we find that only three of the 16 (luminosity-weighted) polarization coefficients are nonzero:

$$\hat{C}_1^w = 2\frac{M_t^2}{\hat{s}}(1 + \beta^2), \quad \hat{C}_2^w = 4\frac{M_t^2}{\hat{s}}\beta, \quad \hat{C}_{13}^w = -2\frac{M_t^2}{\hat{s}}(1 - \beta^2). \quad (42)$$

Consequently, based on Eqs. (22), (23), (24), and (25), we find that only the following polarization vectors and spin correlations are nonvanishing:

$$B_k^+ = -B_k^- = \frac{\hat{C}_2^w}{\hat{C}_1^w} = \frac{2\beta}{1 + \beta^2}, \quad C_{nn} = C_{rr} = \frac{\hat{C}_{13}^w}{\hat{C}_1^w} = -\frac{1 - \beta^2}{1 + \beta^2} < 0, \quad C_{kk} = -\frac{\hat{C}_1^w}{\hat{C}_1^w} = -1 < 0. \quad (43)$$

Substituting these polarization vectors and spin correlations into Eq. (5)<sup>5</sup>, we obtain the following spin density matrices  $\rho$  and  $\rho^{T_B}$ :

$$\rho = \frac{1}{2(1 + \beta^2)} \left( \begin{array}{cc|cc} 0 & 0 & 0 & 0 \\ 0 & (1 + \beta)^2 & -(1 - \beta^2) & 0 \\ \hline 0 & -(1 - \beta^2) & (1 - \beta)^2 & 0 \\ 0 & 0 & 0 & 0 \end{array} \right); \quad \rho^{T_B} = \frac{1}{2(1 + \beta^2)} \left( \begin{array}{cc|cc} 0 & 0 & 0 & -(1 - \beta^2) \\ 0 & (1 + \beta)^2 & 0 & 0 \\ \hline 0 & 0 & (1 - \beta)^2 & 0 \\ -(1 - \beta^2) & 0 & 0 & 0 \end{array} \right). \quad (44)$$

Note that  $\rho^{T_B}$  is obtained by transposing the four  $2 \times 2$  blocks of  $\rho$ . In the limit  $\beta \rightarrow 0$ ,  $B_i^+ = B_j^- = 0$  and  $C_{ij} = -\delta_{ij}$ ; consequently, the spin density matrix  $\rho$  represents a pure singlet state with  $J^P = 0^-$ ,<sup>6</sup> satisfying  $\rho^2 = \rho$ , which indicates perfectly anti-correlated spins between the two spin-1/2 particles [1]. The four eigenvalues of  $\rho^{T_B}$  are

$$\pm \frac{1 - \beta^2}{2(1 + \beta^2)}, \quad \frac{(1 - \beta)^2}{2(1 + \beta^2)}, \quad \frac{(1 + \beta)^2}{2(1 + \beta^2)}. \quad (45)$$

<sup>5</sup>We identify that  $1 = \hat{n}$ ,  $2 = \hat{r}$ , and  $3 = \hat{k}$ .

<sup>6</sup>For a CP-even scalar with  $J^P = 0^+$ ,  $B_i^+ = B_j^- = 0$ ,  $C_{nn} = C_{rr} = +1$ , and  $C_{kk} = -1$ .

We observe that  $\rho^{TB}$  has three positive eigenvalues. However, the fourth eigenvalue is always negative and approaches 0 as  $\beta \rightarrow 1$ , yielding the negativity

$$\mathcal{N}[\rho] = \frac{1 - \beta^2}{2(1 + \beta^2)} > 0. \quad (46)$$

This result guarantees that quantum entanglement is present throughout the entire  $(\cos \Theta, \sqrt{\hat{s}})$  plane for  $w^{++} = 1$ , as a consequence of the Peres-Horodecki criterion (6).

The  $4 \times 4$  auxiliary matrix  $R$ , which is closely linked to concurrence  $\mathcal{C}[\rho]$  of the system, is given by

$$R = \rho (\sigma_2 \otimes \sigma_2) \rho^* (\sigma_2 \otimes \sigma_2) = \frac{1}{2(1 + \beta^2)^2} \left( \begin{array}{cc|cc} 0 & 0 & 0 & 0 \\ 0 & (1 - \beta^2)^2 & -(1 + \beta)^2(1 - \beta^2) & 0 \\ \hline 0 & -(1 - \beta)^2(1 - \beta^2) & (1 - \beta^2)^2 & 0 \\ 0 & 0 & 0 & 0 \end{array} \right), \quad (47)$$

when  $w^{++} = 1$ . Its four eigenvalues are

$$r_1^2 = \frac{(1 - \beta^2)^2}{(1 + \beta^2)^2}, \quad r_2^2 = r_3^2 = r_4^2 = 0. \quad (48)$$

As a consequence of the analytic results derived above, we can obtain the following expression for concurrence  $\mathcal{C}[\rho]$  of the quantum state:

$$\mathcal{C}[\rho] = r_1 = \frac{1 - \beta^2}{1 + \beta^2} = 2\mathcal{N}[\rho] > 0. \quad (49)$$

This result further confirms quantum entanglement throughout the  $(\cos \Theta, \sqrt{\hat{s}})$  plane for  $w^{++} = 1$ , consistent with Eq. (8).

Concerning the CHSH criterion, as expressed in Eq. (10), for the Bell nonlocality parameter  $m_{12}$ , we find that:

$$C = \text{diag} \left( -\frac{1 - \beta^2}{1 + \beta^2}, -\frac{1 - \beta^2}{1 + \beta^2}, -1 \right), \quad (50)$$

which leads to the sum of the two largest eigenvalues of the matrix  $CC^T$ :

$$m_{12} = m_1 + m_2 = 1 + \frac{(1 - \beta^2)^2}{(1 + \beta^2)^2} = 1 + (\mathcal{C}[\rho])^2 > 1. \quad (51)$$

This inequality also ensures Bell inequality violation across the entire  $(\cos \Theta, \sqrt{\hat{s}})$  plane for  $w^{++} = 1$ . For the entanglement marker  $D$  in Eq. (12), we have

$$D = \frac{\Delta E}{3} = \frac{1}{3} (C_{nn} - |C_{rr} + C_{kk}|) = \frac{1}{3} \text{Tr}[C] = \frac{1}{3} \left( -1 - 2 \frac{1 - \beta^2}{1 + \beta^2} \right) = \frac{1}{3} (-1 - 2\mathcal{C}[\rho]) < -\frac{1}{3}. \quad (52)$$

because  $C_{nn} - |C_{rr} + C_{kk}| = \text{Tr}[C]$  with  $C_{nn,rr,kk} < 0$ .

The left and middle panels of Fig. 4 show the contour regions in the  $(\cos \Theta, \sqrt{\hat{s}})$  plane for negativity  $\mathcal{N}[\rho]$  (7) (upper left), concurrence  $\mathcal{C}[\rho]$  (8) (upper right), the Bell nonlocality parameter  $m_{12}$  (10) (lower left), and the entanglement marker  $D$  (12) (lower right), for perfectly polarized colliding photons with  $w^{++} = 1$ .<sup>7</sup> The upper frame of the right panel presents plots of  $m_{12}$ ,  $\mathcal{C}[\rho]$ ,  $\mathcal{N}[\rho]$ , and  $D$  (arranged from top to bottom) as functions of  $\sqrt{\hat{s}}$ . The region  $2M_t < \sqrt{\hat{s}} < 500$  GeV is magnified in the lower frame. We observe that all the entanglement quantifiers are essentially independent of  $\cos \Theta$ . At  $\sqrt{\hat{s}} = 2M_t$ , they reach values indicative of maximal entanglement and approach the boundary between entanglement and separability as  $\sqrt{\hat{s}} \rightarrow \infty$ . Importantly, all four criteria for quantum entanglement and Bell inequality violation, namely  $\mathcal{N}[\rho] > 0$ ,  $\mathcal{C}[\rho] > 0$ ,  $m_{12} > 1$ , and  $-D > 1/3$ , are satisfied across the entire range of  $\sqrt{\hat{s}}$ , although the entanglement quantifiers decrease rapidly with increasing  $\sqrt{\hat{s}}$ . This behavior is precisely captured by the analytical expressions derived

<sup>7</sup>We plot  $-D$  instead of  $+D$  so that larger values of  $\mathcal{N}[\rho]$ ,  $\mathcal{C}[\rho]$ ,  $m_{12}$ , and  $-D$  consistently indicate stronger entanglement.

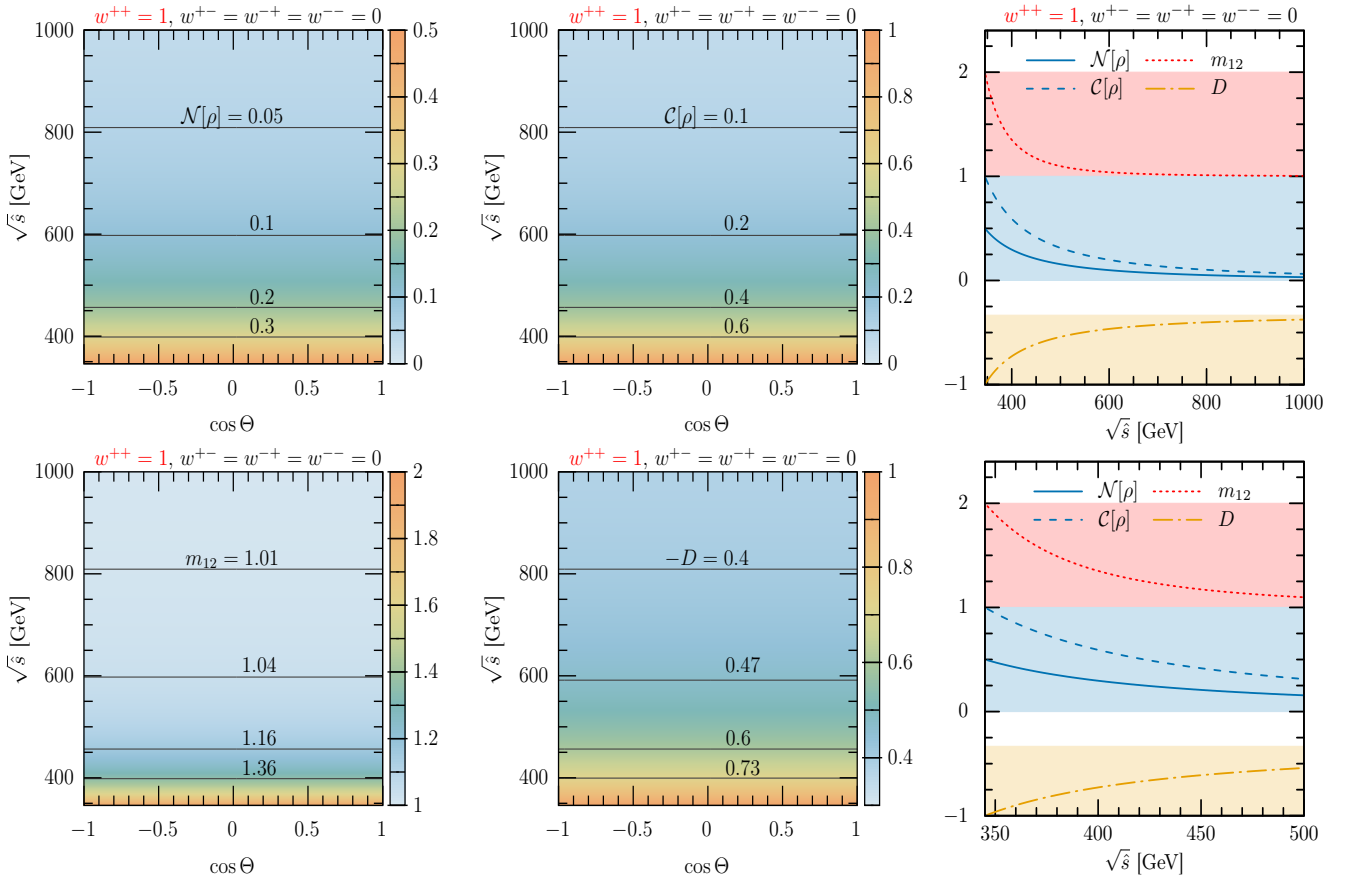


FIG. 4. **Quantum entanglement with  $w^{\pm\pm} = 1$ :** (Left and Middle) Contour regions in the  $(\cos \Theta, \sqrt{\hat{s}})$  plane for negativity  $\mathcal{N}[\rho]$  (upper-left), concurrence  $\mathcal{C}[\rho]$  (upper-right), the Bell nonlocality parameter  $m_{12}$ , and the entanglement marker  $D$  (lower-right). (Right) Bell nonlocality parameter  $m_{12}$ , concurrence  $\mathcal{C}[\rho]$ , negativity  $\mathcal{N}[\rho]$ , and entanglement marker  $D$  as functions of  $\sqrt{\hat{s}}$ , from top to bottom. Shaded regions satisfy  $m_{12} > 1$ ,  $\mathcal{C}[\rho] > 0$ ,  $\mathcal{N}[\rho] > 0$ , and  $D < -1/3$ , indicating quantum entanglement and violation of the Bell inequality. The lower frame magnifies the region  $2M_t < \sqrt{\hat{s}} < 500$  GeV.

above, demonstrating the utility of the spin density matrix formalism for a two-qubit system. Constructed from the amplitude level, the formalism is particularly useful at incorporating polarization effects at colliders.

Finally, we observe that, for  $w^{--} = 1$  and  $w^{++} = w^{+-} = w^{-+} = 0$ , the luminosity-weighted coefficients  $\widehat{C}_1^w$  and  $\widehat{C}_{13}^w$  are unaffected, whereas  $\widehat{C}_2^w$  changes sign. Consequently, the entanglement quantifiers  $\mathcal{N}[\rho]$ ,  $\mathcal{C}[\rho]$ ,  $m_{12}$ , and  $D$  remain the same, ensuring quantum entanglement throughout the  $(\cos \Theta, \sqrt{\hat{s}})$  plane, as in the  $w^{++} = 1$  case.

### C. Perfectly polarized colliding photons with $w^{\pm\mp} = 1$

The situation becomes more complex when the colliding photons have opposite helicities, with  $w^{\pm\mp} = 1$  and  $w^{++} = w^{--} = w^{\mp\pm} = 0$ . In this case, the luminosity-weighted polarization coefficients  $\widehat{C}_i^w$  receive contributions from all four reduced amplitudes with  $\sigma\bar{\sigma} = ++, --, +-,$  and  $-+$ . To illustrate, consider the specific case where  $w^{+-} = 1$  at  $\cos \Theta = 0$  and  $\sin \Theta = 1$ . For  $\lambda_1 = -\lambda_2 = +1$ , the luminosity-weighted polarization coefficients  $\widehat{C}_i^w$  receive contributions from the following reduced amplitudes (see Table I):

$$\langle ++; +-\rangle = -\frac{2M_t}{\sqrt{\hat{s}}} \beta, \quad \langle --; +-\rangle = \frac{2M_t}{\sqrt{\hat{s}}} \beta; \quad \langle -+; +-\rangle = \beta, \quad \langle +-; +-\rangle = -\beta. \quad (53)$$

Specifically, we observe that the following 5 luminosity-weighted polarization coefficients are nonzero:<sup>8</sup>

$$\widehat{C}_1^w = 2 \frac{M_t^2}{\hat{s}} \beta^2, \quad \widehat{C}_3^w = \frac{\beta^2}{2}, \quad \widehat{C}_5^w = -\frac{2M_t}{\sqrt{\hat{s}}} \beta^2, \quad \widehat{C}_{13}^w = 2 \frac{M_t^2}{\hat{s}} \beta^2, \quad \widehat{C}_{15}^w = \frac{\beta^2}{2}. \quad (54)$$

Therefore, based on Eqs. (22), (23), (24), and (25), we observe that only the following polarization vectors and spin correlations are nonvanishing:

$$B_r^+ = B_r^- = \frac{4M_t \sqrt{\hat{s}}}{\hat{s} + 4M_t^2}, \quad C_{nn} = -\frac{\hat{s} - 4M_t^2}{\hat{s} + 4M_t^2} < 0, \quad C_{rr} = 1 > 0, \quad C_{kk} = -C_{nn} > 0. \quad (55)$$

We note that the diagonal  $3 \times 3$  spin correlation matrix, given by  $C = \text{diag}(C_{nn}, C_{rr}, C_{kk})$ , leads to

$$m_{12}|_{\cos \Theta=0} = 1 + \frac{(\hat{s} - 4M_t^2)^2}{(\hat{s} + 4M_t^2)^2} > 1; \quad D|_{\cos \Theta=0} = \frac{1}{3}(C_{nn} - |C_{rr} + C_{kk}|) = \frac{1}{3} \left( -1 - 2 \frac{\hat{s} - 4M_t^2}{\hat{s} + 4M_t^2} \right) < -\frac{1}{3}. \quad (56)$$

In fact, for  $w^{\pm\mp} = 1$ , we find that the entanglement quantifiers are

$$\mathcal{N}[\rho] = \frac{\beta^2 \sin^2 \Theta}{2(2 - \beta^2 \sin^2 \Theta)}, \quad \mathcal{C}[\rho] = 2\mathcal{N}[\rho], \quad m_{12} = 1 + (\mathcal{C}[\rho])^2, \quad D = \frac{1}{3}(-1 - 2\mathcal{C}[\rho]). \quad (57)$$

For a given value of  $\sqrt{\hat{s}}$ , the strongest entanglement occurs at  $\sin \Theta = 1$ , where  $\mathcal{C}[\rho] = 2\mathcal{N}[\rho] = \beta^2/(2 - \beta^2) = (\hat{s} - 4M_t^2)/(\hat{s} + 4M_t^2)$ . In contrast to the  $w^{\pm\pm} = 1$  case, we find that the boundary between entanglement and separability

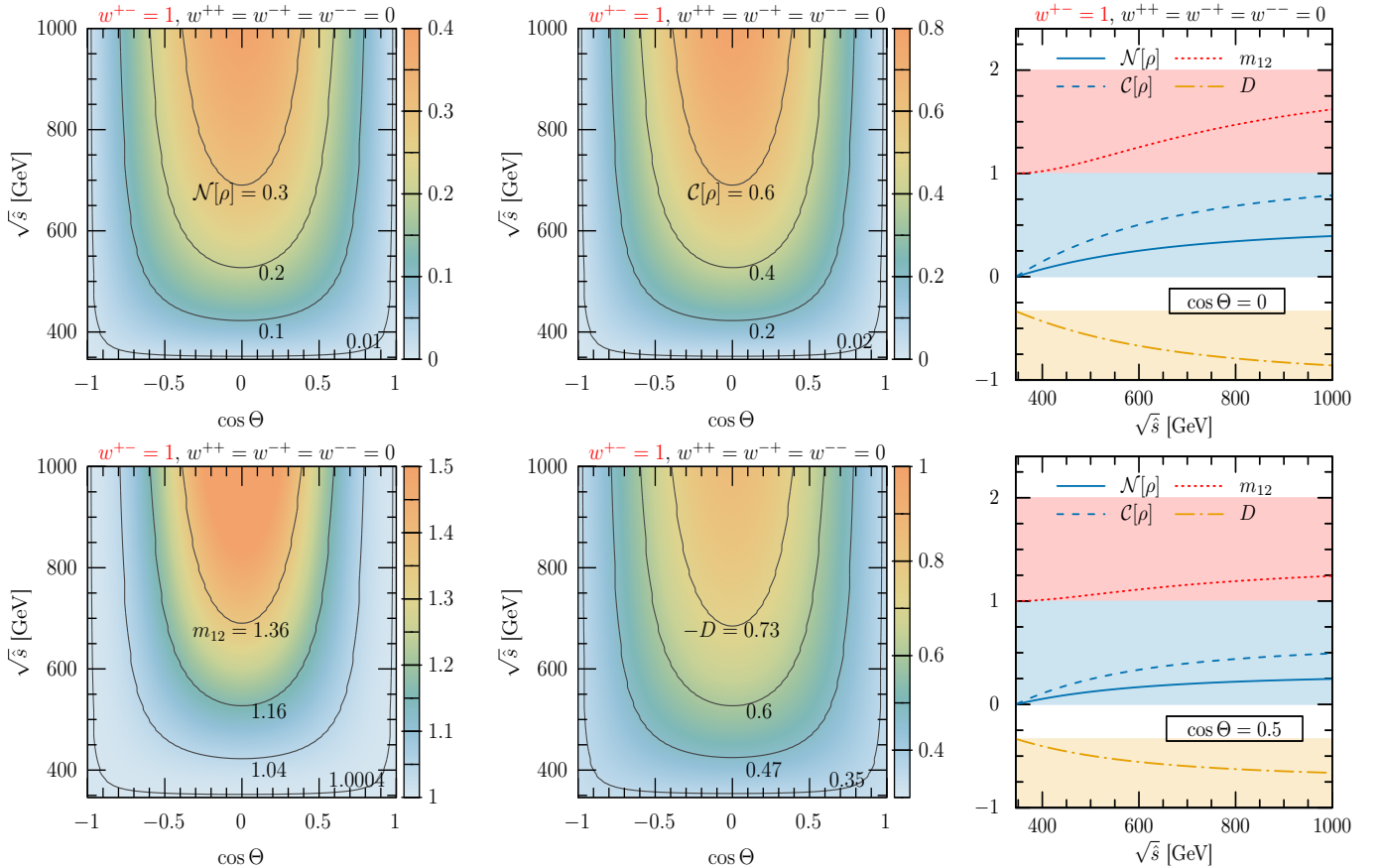


FIG. 5. **Quantum entanglement with  $w^{\pm\mp} = 1$ :** Same as in Fig. 4 but for  $w^{\pm\mp} = 1$  and, in the right panel, for  $\cos \Theta = 0$  and  $0.5$ .

<sup>8</sup>Note that if  $w^{-+} = 1$ ,  $\widehat{C}_5^w$  changes sign, whereas the other coefficients are unaffected.

is located at  $\sqrt{\hat{s}} = 2M_t$  and all entanglement quantifiers approach their maximal values as  $\sqrt{\hat{s}} \rightarrow \infty$ , when  $w^{\pm\mp} = 1$ . In this limit of  $\sqrt{\hat{s}} \rightarrow \infty$ ,  $B_r^+ = B_r^- = 0$  and  $C = \text{diag}(-1, 1, 1)$  at  $\cos \Theta = 0$ ; consequently, the spin density matrix  $\rho$  represents a pure triplet state.

Similar to Fig. 4, but now for  $w^{+-} = 1$ , the left and middle panels of Fig. 5 display contour regions in the  $(\cos \Theta, \sqrt{\hat{s}})$  plane for negativity  $\mathcal{N}[\rho]$ , concurrence  $\mathcal{C}[\rho]$ , the Bell nonlocality parameter  $m_{12}$ , and the entanglement marker  $D$ . The right panel shows the  $\sqrt{\hat{s}}$  dependence of these quantities at  $\cos \Theta = 0$  (upper) and  $\cos \Theta = 0.5$  (lower). Note that  $\mathcal{N}[\rho]$ ,  $\mathcal{C}[\rho]$ ,  $m_{12}$ , and  $-D$  increase slowly as  $\sqrt{\hat{s}}$  increases, in contrast to the same-helicity case, where these quantities decrease rapidly as  $\sqrt{\hat{s}}$  moves away from the  $2M_t$  threshold. This makes opposite-helicity photons the preferred choice for entanglement measurement over a broad range of  $\sqrt{\hat{s}}$ , particularly in the high- $\sqrt{\hat{s}}$  region, whereas same-helicity photons remain advantageous near the  $2M_t$  threshold.

#### D. Polarized colliding photons with $\sqrt{s} = 500$ GeV and $P_e = \tilde{P}_e = +1$

To address the case of imperfectly polarized colliding photons near the  $2M_t$  threshold, we consider the case where

$$\sqrt{s} = 500 \text{ GeV}; \quad P_e = -P_c = \tilde{P}_e = -\tilde{P}_c = +1. \quad (58)$$

In this case, the invariant mass of the  $t\bar{t}$  system is constrained by  $2M_t < \sqrt{\hat{s}} \lesssim 410$  GeV, and the colliding photons are polarized with  $w^{++} \gtrsim 0.7$ ,  $w^{+-} = w^{-+} \lesssim 0.15$ , and  $w^{--} \lesssim 3 \times 10^{-3}$  (see the right panel of Fig. 2). We find that quantum entanglement is observable throughout the entire  $(\cos \Theta, \sqrt{\hat{s}})$  plane, as this case can be well approximated by the perfectly polarized scenario with  $w^{++} = 1$ .

Figure 6 displays the contour regions for negativity  $\mathcal{N}[\rho]$ , concurrence  $\mathcal{C}[\rho]$ , the Bell nonlocality parameter  $m_{12}$ , and the entanglement marker  $D$ . We recall that, for given values of  $\cos \Theta$  and  $\sqrt{\hat{s}}$ , the entanglement quantifiers are calculated using the spin density matrix  $\rho$  from Eq. (22), with  $\hat{C}_i$  replaced by  $\hat{C}_i^w$  in Eqs. (23), (24), and (25). The luminosity-

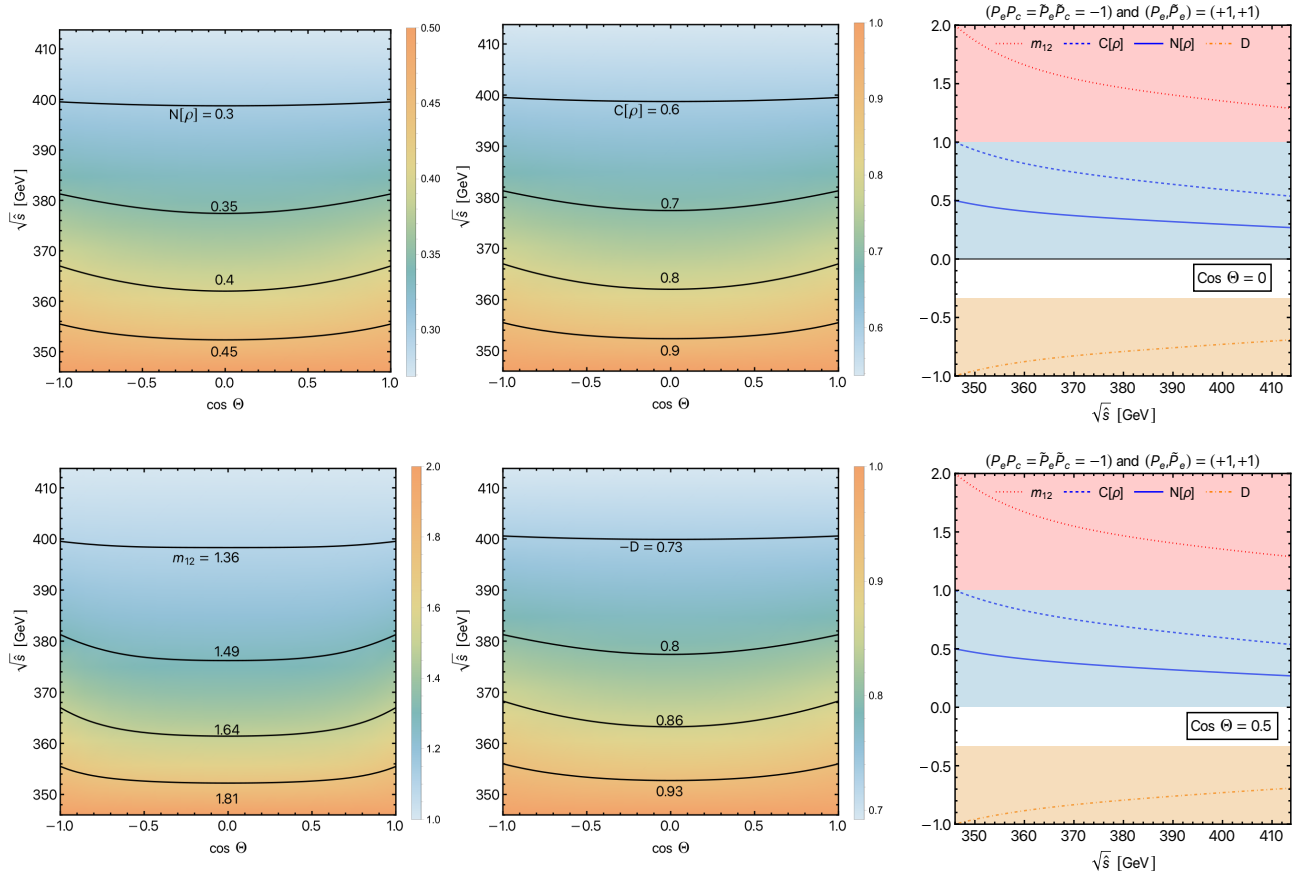


FIG. 6. Quantum entanglement with  $\sqrt{s} = 500$  GeV and  $P_e = \tilde{P}_e = +1$ : Same as in Fig. 5 but for  $\sqrt{s} = 500$  GeV and  $P_e = -P_c = \tilde{P}_e = -\tilde{P}_c = +1$ .

weighted polarization coefficients  $\widehat{C}_i^w$  are defined in Eq. (37). For example, the  $kk$  element of the  $3 \times 3$  spin correlation matrix  $C$  is given by

$$C_{kk}(\sqrt{\hat{s}}, \cos \Theta) = \frac{\widehat{C}_{kk}}{\widehat{A}} = \frac{-\widehat{C}_1^w + \widehat{C}_3^w}{\widehat{C}_1^w + \widehat{C}_3^w}. \quad (59)$$

Since  $w^{++} \gtrsim 0.7$  with  $\sqrt{\hat{s}} = 500$  GeV, the accessible range is confined to  $\sqrt{\hat{s}} \lesssim 410$  GeV, corresponding to the narrow region near threshold in Fig. 4. We observe that all four entanglement quantifiers are nearly independent of  $\cos \Theta$ . At  $\sqrt{\hat{s}} = 2M_t$ , they attain their maximal entanglement values: negativity  $\mathcal{N}[\rho] = 1/2$ , concurrence  $\mathcal{C}[\rho] = 1$ , the Bell nonlocality parameter  $m_{12} = 2$ , and  $D = -1$ .

### E. Polarized colliding photons with $\sqrt{s} = 1$ TeV and $P_e = -\tilde{P}_e = +1$

To address the high- $\sqrt{\hat{s}}$  regime and to cover a broader range of  $\sqrt{\hat{s}}$ , we now consider the case where

$$\sqrt{s} = 1 \text{ TeV}; \quad P_e = -P_c = -\tilde{P}_e = +\tilde{P}_c = +1. \quad (60)$$

In this scenario, the invariant mass of the  $t\bar{t}$  system is constrained to  $2M_t < \sqrt{\hat{s}} \lesssim 820$  GeV. In the region  $2M_t < \sqrt{\hat{s}} \lesssim 400$  GeV, the colliding photons are polarized with  $w^{+-} \lesssim 0.01$ ,  $w^{++} = w^{--} \sim 0.4$ , and  $w^{-+} \sim 0.2$  (see the right panel of Fig. 2). In contrast, when  $\sqrt{\hat{s}} \gtrsim 680$  GeV, they become  $w^{+-} \gtrsim 0.7$ ,  $w^{++} = w^{--} \lesssim 0.15$ , and  $w^{-+} \lesssim 3 \times 10^{-3}$ . Therefore, the high- $\sqrt{\hat{s}}$  region is expected to be well approximated by the perfectly polarized scenario with  $w^{+-} = 1$ , whereas near the  $2M_t$  threshold, the behavior likely falls between the unpolarized case and the perfectly polarized scenario with  $w^{\pm\pm} = 1$ .

Figure 7 presents the contour regions for negativity  $\mathcal{N}[\rho]$ , concurrence  $\mathcal{C}[\rho]$ , the Bell nonlocality parameter  $m_{12}$ , and the

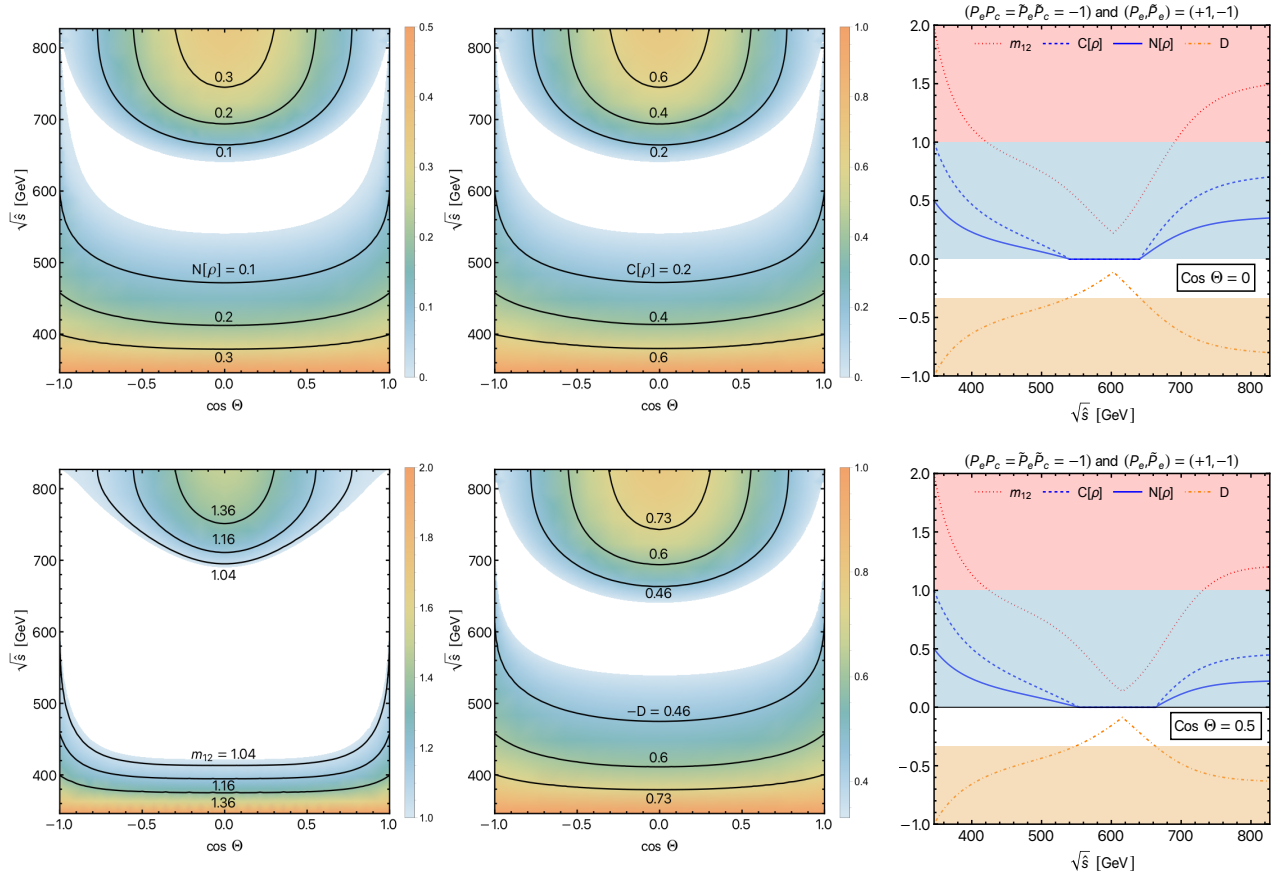


FIG. 7. **Quantum entanglement with  $\sqrt{s} = 1$  TeV and  $P_e = -\tilde{P}_e = +1$ :** Same as in Fig. 6 but for  $\sqrt{s} = 1$  TeV and  $P_e = -P_c = -\tilde{P}_e = \tilde{P}_c = +1$ .

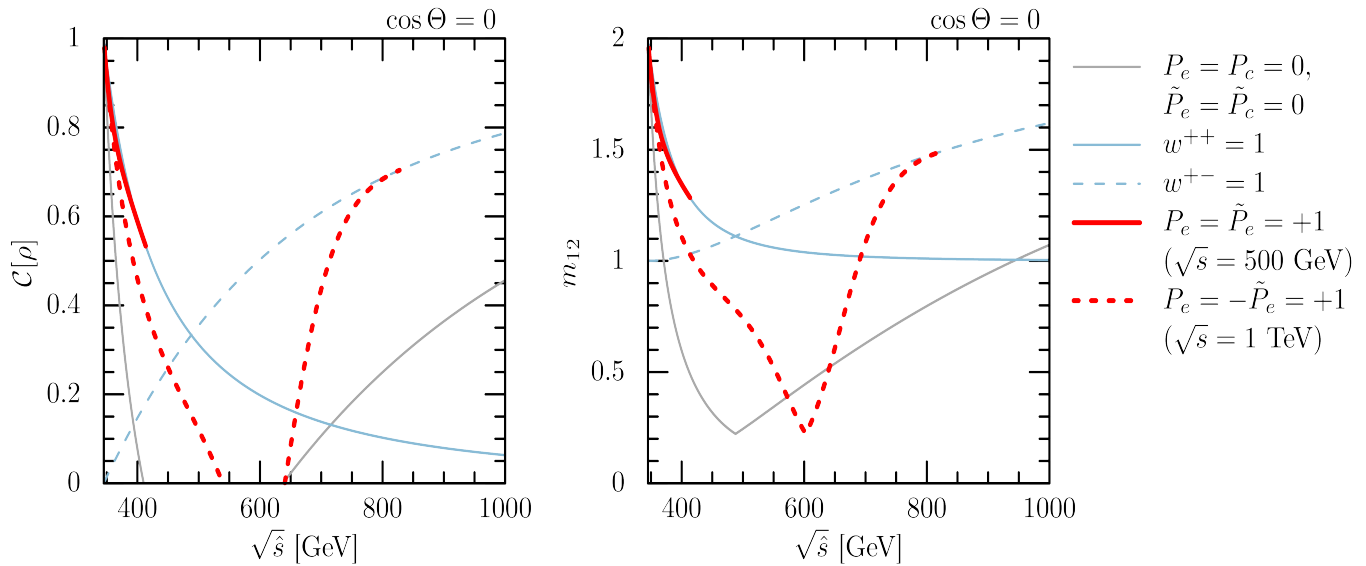


FIG. 8. **Comparisons of quantum entanglement and Bell inequality violation:** Concurrence  $\mathcal{C}[\rho]$  (left) and Bell nonlocality parameter  $m_{12}$  (right) as functions of  $\sqrt{\hat{s}}$  at  $\cos \Theta = 0$  for unpolarized photons with  $P_e = P_c = \tilde{P}_e = \tilde{P}_c = 0$  (black solid), perfectly polarized same-helicity photons (blue solid), and perfectly polarized opposite-helicity photons (blue dashed). Thick solid and dashed red curves correspond to  $P_e = -P_c = \tilde{P}_e = -\tilde{P}_c = +1$  ( $\sqrt{s} = 500$  GeV) and  $P_e = -P_c = -\tilde{P}_e = +\tilde{P}_c = +1$  ( $\sqrt{s} = 1$  TeV), respectively.

entanglement marker  $D$ , along with their dependence on  $\sqrt{\hat{s}}$ . A key difference from the perfectly polarized cases and the  $\sqrt{s} = 500$  GeV case is that quantum entanglement and Bell inequality violation are not observed throughout the entire  $(\cos \Theta, \sqrt{\hat{s}})$  region. Instead, along the  $\cos \Theta = 0$  line, quantum entanglement ( $\mathcal{N}[\rho] > 0$  or  $\mathcal{C}[\rho] > 0$ ) is observed in the regions  $\sqrt{\hat{s}} \lesssim 540$  GeV and  $\sqrt{\hat{s}} \gtrsim 640$  GeV. Compared to the unpolarized case (Fig. 3), where the corresponding regions are  $\sqrt{\hat{s}} \lesssim 410$  GeV and  $\sqrt{\hat{s}} \gtrsim 640$  GeV, the entangled region is extended at lower  $\sqrt{\hat{s}}$  in this polarized scenario. Similarly, along the  $\cos \Theta = 0$  line, Bell inequality violation ( $m_{12} > 1$ ) is observed in the regions  $\sqrt{\hat{s}} \lesssim 420$  GeV and  $\sqrt{\hat{s}} \gtrsim 690$  GeV. In contrast to the unpolarized case, where Bell inequality violation occurs only for  $\sqrt{\hat{s}} \lesssim 370$  GeV and  $\sqrt{\hat{s}} \gtrsim 950$  GeV, the Bell nonlocality region is significantly extended in both the low- and high- $\sqrt{\hat{s}}$  regions in this polarized scenario. It is worth noting in Fig. 7 that the criterion  $D = \Delta_E/3 < -1/3$  indeed provides a sufficient condition for entanglement. This is evident by comparing the unshaded (white) separable region, where  $\mathcal{N}[\rho] = 0$  or  $\mathcal{C}[\rho] = 0$ , with the region where  $-D \leq 1/3$ , especially at large  $|\cos \Theta|$ . We observe that the separable region shifts toward larger  $\sqrt{\hat{s}}$  and shrinks as  $\cos \Theta$  deviates from 0.

Before concluding, we compare the results obtained in our numerical analysis regarding the impact of colliding-photon polarization on quantum entanglement and Bell inequality violation. Figure 8 shows the concurrence  $\mathcal{C}[\rho]$  (left) and the Bell nonlocality parameter  $m_{12}$  (right) as functions of  $\sqrt{\hat{s}}$ , at  $\cos \Theta = 0$ . In the unpolarized case with  $P_e = P_c = \tilde{P}_e = \tilde{P}_c = 0$  (black solid line), quantum entanglement is observed only near the  $2M_t$  threshold and for  $\sqrt{\hat{s}} \gtrsim 640$  GeV, where  $\mathcal{C}[\rho] > 0$ . The Bell nonlocality range ( $m_{12} > 1$ ) is narrower.

When the colliding photons are perfectly polarized (blue solid and dashed lines), quantum entanglement and the violation of the Bell inequality can be observed across the entire range of  $\sqrt{\hat{s}}$ . Notably, the same-helicity and opposite-helicity cases exhibit complementary behavior. The same-helicity configuration demonstrates particular advantages near the  $2M_t$  threshold, while the opposite-helicity case shows superior performance both across a broad range of  $\sqrt{\hat{s}}$  and specifically in the high- $\sqrt{\hat{s}}$  regime. To examine more realistic scenarios, we consider two specific polarization configurations:  $P_e = -P_c = \tilde{P}_e = -\tilde{P}_c = +1$  and  $P_e = -P_c = -\tilde{P}_e = +\tilde{P}_c = +1$ , evaluated at  $\sqrt{s} = 500$  GeV and 1 TeV, respectively. The first case with  $\sqrt{s} = 500$  GeV is well approximated by the perfectly polarized same-helicity case, as shown by the thick solid red lines in Fig. 8. Conversely, the second case with  $\sqrt{s} = 1$  TeV closely matches the perfectly polarized opposite-helicity case for  $\sqrt{\hat{s}} \gtrsim 750$  GeV, as illustrated by the thick dashed red lines in Fig. 8. Outside this high-energy region, the behavior falls intermediate between the unpolarized and perfectly polarized cases. In summary, our numerical analysis demonstrates that the ability to control photon polarizations at a PLC substantially improves the prospects for observing quantum entanglement and the violation of the Bell inequality.

## VI. CONCLUSIONS AND SUMMARY

A PLC, the two-photon collision mode of a linear  $e^+e^-$  collider, provides great opportunities to observe quantum entanglement and the violation of the Bell inequality. The polarizations of the colliding photons can be controlled through polarized initial electrons and positrons combined with polarized laser beams. This capability can significantly enhance the magnitudes of the quantum entanglement quantifiers such as negativity  $\mathcal{N}[\rho]$  (7), concurrence  $\mathcal{C}[\rho]$  (8), the Bell nonlocality parameter  $m_{12}$  (10), and the entanglement marker  $D$  (12). To analyze the impact of colliding-photon polarizations on the observation of quantum entanglement through top-quark pair production at a PLC,  $\gamma\gamma \rightarrow t\bar{t}$ , we have developed a formalism for the spin density matrix of a two-qubit system constructed from the helicity amplitudes.

Once the spin density matrix is given, the criteria for quantum entanglement and the violation of the Bell inequality are readily evaluated. The 16 polarization coefficients  $\hat{C}_i$  given in Appendix A in terms of the reduced helicity amplitudes (Table I) determine the spin density matrix  $\rho$  in Eq. (22) through the polarization vectors (23) and spin correlations (24) together with the normalization factor (25). When the colliding photons are polarized, one can obtain the spin density matrix by using the luminosity-weighted polarization coefficients  $\hat{C}_i^w$  in Eq. (37). We emphasize that our formalism for the spin density matrix of a two-qubit system is not only useful for the analysis of polarized-particle collisions but also generically applicable to any system composed of two spin-1/2 particles beyond LO and/or beyond the SM. It also helps classify the polarization vectors and spin correlations of top quarks according to their P, CP, and  $\text{CPT}$  parities.

Through our numerical analysis, we clearly show that the capability of controlling colliding-photon polarizations at a PLC significantly enhances the chances to observe quantum entanglement and the violation of the Bell inequality compared to the unpolarized case, as illustrated in Fig. 8. Based on our numerical analysis, we highlight the following key points:

1. In the unpolarized case with  $P_e = P_c = \tilde{P}_e = \tilde{P}_c = 0$ , quantum entanglement and Bell inequality violation can be observed near the  $2M_t$  threshold and only for  $\sqrt{\hat{s}} \gtrsim 640$  GeV and  $\gtrsim 950$  GeV, respectively, see Fig. 3.
2. When the colliding photons are perfectly polarized with the same helicities, quantum entanglement and Bell inequality violation can be observed across the entire region of  $\cos\Theta$  and  $\sqrt{\hat{s}}$ , see Fig. 4. The quantum entanglement quantifiers do not depend on  $\cos\Theta$ , and their magnitudes quickly *decrease* as  $\sqrt{\hat{s}}$  increases.
3. When the colliding photons are perfectly polarized with opposite helicities, quantum entanglement and Bell inequality violation can be observed again across the entire region of  $\cos\Theta$  and  $\sqrt{\hat{s}}$ , see Fig. 5. The magnitudes of the quantum entanglement quantifiers take their largest values along the  $\cos\Theta = 0$  line, and they *increase* as  $\sqrt{\hat{s}}$  increases.
4. For  $\sqrt{s} = 500$  GeV with  $P_e = \tilde{P}_e = +1$ ,  $x = 4.8$ , and  $P_e P_c = \tilde{P}_e \tilde{P}_c = -1$ ,  $\sqrt{\hat{s}}$  ranges from  $2M_t$  to 410 GeV. The colliding photons are polarized with  $w^{++} \gtrsim 0.7$ ,  $w^{+-} = w^{-+} \lesssim 0.15$ , and  $w^{--} \lesssim 3 \times 10^{-3}$ . Quantum entanglement and Bell inequality violation can be observed across the entire region of  $\cos\Theta$  and  $\sqrt{\hat{s}}$ , see Fig. 6. This case is well approximated by the perfectly polarized *same*-helicity configuration.
5. For  $\sqrt{s} = 1$  TeV with  $P_e = -\tilde{P}_e = +1$ ,  $x = 4.8$ , and  $P_e P_c = \tilde{P}_e \tilde{P}_c = -1$ ,  $\sqrt{\hat{s}}$  ranges from  $2M_t$  to 820 GeV. The magnitudes of the quantum entanglement quantifiers take their largest values along the  $\cos\Theta = 0$  line, see Fig. 7. Along the line, quantum entanglement can be observed in the regions with  $\sqrt{\hat{s}} \lesssim 540$  GeV and  $\sqrt{\hat{s}} \gtrsim 640$  GeV, and Bell inequality violation in the regions with  $\sqrt{\hat{s}} \lesssim 420$  GeV and  $\sqrt{\hat{s}} \gtrsim 690$  GeV. This case is well approximated by the perfectly polarized *opposite*-helicity configuration for  $\sqrt{\hat{s}} \gtrsim 750$  GeV.

In conclusion, the polarization control available at a PLC provides a powerful handle for maximizing quantum entanglement and observing Bell inequality violation in top-quark pair production. The amplitude-level formalism developed in this work, with its process- and model-independent classification of the spin density matrix by P, CP, and  $\text{CPT}$  parities, constitutes a systematic framework directly applicable to other processes and to new-physics searches beyond the SM.

## ACKNOWLEDGMENT

D.W.K. and C.B.P. thank the Asia Pacific Center for Theoretical Physics (APCTP), Pohang, Korea, for their hospitality during the Focus Program (APCTP-2026-F01), from which this work greatly benefited. The work of S.Y.C. was supported by the Basic Science Research Program through the National Research Foundation (NRF) of Korea (No. RS-2022-NR075766) funded by the Ministry of Education. The work of D.W.K. was supported by the NRF grant funded by the Korea government (Ministry of Science and ICT, MSIT) (No. RS-2025-02653237 and No. RS-2025-00562917) and Global - Learning Academic research institution for Master's-PhD students, and Postdocs (LAMP) Program of the NRF grant funded by the Ministry of Education (No. RS-2024-00443714). The work of J.S.L. was supported by the NRF grant

funded by the Korea government (No. RS-2025-23523535). The work of C.B.P. was supported by the NRF grant funded by the Korea government (MSIT) (No. RS-2023-00209974). This work was also supported in part by the NRF of Korea under Grants No. RS-2022-NR070836 and No. RS-2024-00442775.

### Appendix A: Polarization coefficients $\widehat{C}_i$ for $i$ from 1 to 16

This appendix provides the explicit expressions for the 16 polarization coefficients,  $\widehat{C}_i$  (where  $i$  ranges from 1 to 16), in terms of the reduced helicity amplitudes,  $\langle\sigma\bar{\sigma}; \lambda_1\lambda_2\rangle$ . These amplitudes are defined in Eq. (15) and their values for the process under consideration are listed in Table I. The expressions are given as follows:

$$\begin{aligned}
\widehat{C}_1[+++ ] &= \frac{1}{4} \sum_{\lambda_1, \lambda_2 = \pm} [|\langle ++; \lambda_1\lambda_2 \rangle|^2 + |\langle --; \lambda_1\lambda_2 \rangle|^2], \\
\widehat{C}_2[- - -] &= \frac{1}{4} \sum_{\lambda_1, \lambda_2 = \pm} [|\langle ++; \lambda_1\lambda_2 \rangle|^2 - |\langle --; \lambda_1\lambda_2 \rangle|^2], \\
\widehat{C}_3[+ + +] &= \frac{1}{4} \sum_{\lambda_1, \lambda_2 = \pm} [|\langle -+; \lambda_1\lambda_2 \rangle|^2 + |\langle +-; \lambda_1\lambda_2 \rangle|^2], \\
\widehat{C}_4[- + +] &= -\frac{1}{4} \sum_{\lambda_1, \lambda_2 = \pm} [|\langle -+; \lambda_1\lambda_2 \rangle|^2 - |\langle +-; \lambda_1\lambda_2 \rangle|^2], \tag{A.1}
\end{aligned}$$

$$\begin{aligned}
\widehat{C}_5[- + +] &= \frac{1}{4} \Re \sum_{\lambda_1, \lambda_2 = \pm} (\langle ++; \lambda_1\lambda_2 \rangle - \langle --; \lambda_1\lambda_2 \rangle)(\langle -+; \lambda_1\lambda_2 \rangle - \langle +-; \lambda_1\lambda_2 \rangle)^*, \\
\widehat{C}_6[+ + -] &= -\frac{1}{4} \Im \sum_{\lambda_1, \lambda_2 = \pm} (\langle ++; \lambda_1\lambda_2 \rangle - \langle --; \lambda_1\lambda_2 \rangle)(\langle -+; \lambda_1\lambda_2 \rangle + \langle +-; \lambda_1\lambda_2 \rangle)^*, \\
\widehat{C}_7[- - -] &= \frac{1}{4} \Re \sum_{\lambda_1, \lambda_2 = \pm} (\langle ++; \lambda_1\lambda_2 \rangle + \langle --; \lambda_1\lambda_2 \rangle)(\langle -+; \lambda_1\lambda_2 \rangle + \langle +-; \lambda_1\lambda_2 \rangle)^*, \\
\widehat{C}_8[+ - +] &= -\frac{1}{4} \Im \sum_{\lambda_1, \lambda_2 = \pm} (\langle ++; \lambda_1\lambda_2 \rangle + \langle --; \lambda_1\lambda_2 \rangle)(\langle -+; \lambda_1\lambda_2 \rangle - \langle +-; \lambda_1\lambda_2 \rangle)^*, \tag{A.2}
\end{aligned}$$

$$\begin{aligned}
\widehat{C}_9[+ - -] &= \frac{1}{4} \Re \sum_{\lambda_1, \lambda_2 = \pm} (\langle ++; \lambda_1\lambda_2 \rangle + \langle --; \lambda_1\lambda_2 \rangle)(\langle -+; \lambda_1\lambda_2 \rangle - \langle +-; \lambda_1\lambda_2 \rangle)^*, \\
\widehat{C}_{10}[- - +] &= -\frac{1}{4} \Im \sum_{\lambda_1, \lambda_2 = \pm} (\langle ++; \lambda_1\lambda_2 \rangle + \langle --; \lambda_1\lambda_2 \rangle)(\langle -+; \lambda_1\lambda_2 \rangle + \langle +-; \lambda_1\lambda_2 \rangle)^*, \\
\widehat{C}_{11}[+ + +] &= \frac{1}{4} \Re \sum_{\lambda_1, \lambda_2 = \pm} (\langle ++; \lambda_1\lambda_2 \rangle - \langle --; \lambda_1\lambda_2 \rangle)(\langle -+; \lambda_1\lambda_2 \rangle + \langle +-; \lambda_1\lambda_2 \rangle)^*, \\
\widehat{C}_{12}[- + -] &= -\frac{1}{4} \Im \sum_{\lambda_1, \lambda_2 = \pm} (\langle ++; \lambda_1\lambda_2 \rangle - \langle --; \lambda_1\lambda_2 \rangle)(\langle -+; \lambda_1\lambda_2 \rangle - \langle +-; \lambda_1\lambda_2 \rangle)^*, \tag{A.3}
\end{aligned}$$

$$\begin{aligned}
\widehat{C}_{13}[+ + +] &= -\frac{1}{2} \Re \sum_{\lambda_1, \lambda_2 = \pm} [\langle ++; \lambda_1\lambda_2 \rangle \langle --; \lambda_1\lambda_2 \rangle^*], \\
\widehat{C}_{14}[- - +] &= \frac{1}{2} \Im \sum_{\lambda_1, \lambda_2 = \pm} [\langle ++; \lambda_1\lambda_2 \rangle \langle --; \lambda_1\lambda_2 \rangle^*], \\
\widehat{C}_{15}[+ + +] &= -\frac{1}{2} \Re \sum_{\lambda_1, \lambda_2 = \pm} [\langle -+; \lambda_1\lambda_2 \rangle \langle +-; \lambda_1\lambda_2 \rangle^*], \\
\widehat{C}_{16}[- + -] &= -\frac{1}{2} \Im \sum_{\lambda_1, \lambda_2 = \pm} [\langle -+; \lambda_1\lambda_2 \rangle \langle +-; \lambda_1\lambda_2 \rangle^*]. \tag{A.4}
\end{aligned}$$

The entries within the square brackets represent the P, CP, and  $C\tilde{T}$  parities associated with each polarization coefficient.

- 
- [1] See, for example, A. J. Barr, M. Fabbrichesi, R. Floreanini, E. Gabrielli and L. Marzola, “Quantum entanglement and Bell inequality violation at colliders,” *Prog. Part. Nucl. Phys.* **139**, 104134 (2024) doi:10.1016/j.pnpnp.2024.104134 [arXiv:2402.07972 [hep-ph]].
- [2] Y. Afik and J. R. M. de Nova, “Entanglement and quantum tomography with top quarks at the LHC,” *Eur. Phys. J. Plus* **136**, no.9, 907 (2021) doi:10.1140/epjp/s13360-021-01902-1 [arXiv:2003.02280 [quant-ph]].
- [3] M. Fabbrichesi, R. Floreanini and G. Panizzo, “Testing Bell Inequalities at the LHC with Top-Quark Pairs,” *Phys. Rev. Lett.* **127**, no.16, 16 (2021) doi:10.1103/PhysRevLett.127.161801 [arXiv:2102.11883 [hep-ph]].
- [4] G. Aad *et al.* [ATLAS], “Observation of quantum entanglement with top quarks at the ATLAS detector,” *Nature* **633**, no.8030, 542-547 (2024) doi:10.1038/s41586-024-07824-z [arXiv:2311.07288 [hep-ex]].
- [5] A. Hayrapetyan *et al.* [CMS], “Observation of quantum entanglement in top quark pair production in proton–proton collisions at  $\sqrt{s} = 13$  TeV,” *Rept. Prog. Phys.* **87**, no.11, 117801 (2024) doi:10.1088/1361-6633/ad7e4d [arXiv:2406.03976 [hep-ex]].
- [6] A. Hayrapetyan *et al.* [CMS], “Measurements of polarization and spin correlation and observation of entanglement in top quark pairs using lepton+jets events from proton-proton collisions at  $s=13$  TeV,” *Phys. Rev. D* **110**, no.11, 112016 (2024) doi:10.1103/PhysRevD.110.112016 [arXiv:2409.11067 [hep-ex]].
- [7] M. Baumgart and B. Tweedie, “A New Twist on Top Quark Spin Correlations,” *JHEP* **03**, 117 (2013) doi:10.1007/JHEP03(2013)117 [arXiv:1212.4888 [hep-ph]].
- [8] N. A. Tornqvist, “Suggestion for Einstein-podolsky-rosen Experiments Using Reactions Like  $e^+e^- \rightarrow \Lambda\bar{\Lambda} \rightarrow \pi^-p\pi^+\bar{p}$ ,” *Found. Phys.* **11**, 171-177 (1981) doi:10.1007/BF00715204
- [9] N. A. Tornqvist, “The Decay  $J/\psi \rightarrow \Lambda\bar{\Lambda} \rightarrow \pi^-p\pi^+\bar{p}$  as an Einstein-Podolsky-Rosen Experiment,” *Phys. Lett. A* **117**, 1-4 (1986) doi:10.1016/0375-9601(86)90225-2
- [10] P. Privitera, “Decay correlations in  $e^+e^- \rightarrow \tau^+\tau^-$  as a test of quantum mechanics,” *Phys. Lett. B* **275**, 172-180 (1992) doi:10.1016/0370-2693(92)90872-2
- [11] S. A. Abel, M. Dittmar and H. K. Dreiner, “Testing locality at colliders via Bell’s inequality?,” *Phys. Lett. B* **280**, 304-312 (1992) doi:10.1016/0370-2693(92)90071-B
- [12] A. J. Barr, “Testing Bell inequalities in Higgs boson decays,” *Phys. Lett. B* **825**, 136866 (2022) doi:10.1016/j.physletb.2021.136866 [arXiv:2106.01377 [hep-ph]].
- [13] M. Fabbrichesi, R. Floreanini and E. Gabrielli, “Constraining new physics in entangled two-qubit systems: top-quark, tau-lepton and photon pairs,” *Eur. Phys. J. C* **83**, no.2, 162 (2023) doi:10.1140/epjc/s10052-023-11307-2 [arXiv:2208.11723 [hep-ph]].
- [14] M. M. Altakach, P. Lamba, F. Maltoni, K. Mawatari and K. Sakurai, “Quantum information and CP measurement in  $H \rightarrow \tau^+\tau^-$  at future lepton colliders,” *Phys. Rev. D* **107**, no.9, 093002 (2023) doi:10.1103/PhysRevD.107.093002 [arXiv:2211.10513 [hep-ph]].
- [15] M. Fabbrichesi, R. Floreanini, E. Gabrielli and L. Marzola, “Bell inequalities and quantum entanglement in weak gauge boson production at the LHC and future colliders,” *Eur. Phys. J. C* **83**, no.9, 823 (2023) doi:10.1140/epjc/s10052-023-11935-8 [arXiv:2302.00683 [hep-ph]].
- [16] M. Fabbrichesi, R. Floreanini, E. Gabrielli and L. Marzola, “Bell inequality is violated in  $B_0 \rightarrow J/\psi K^*(892)0$  decays,” *Phys. Rev. D* **109**, no.3, L031104 (2024) doi:10.1103/PhysRevD.109.L031104 [arXiv:2305.04982 [hep-ph]].
- [17] Y. Zhang, B. H. Zhou, Q. B. Liu, T. A. Wu, S. Li, T. Han, S. C. Hsu and M. Low, “Entanglement and Bell Nonlocality in  $\tau^+\tau^-$  at the LHC using Machine Learning for Neutrino Reconstruction,” [arXiv:2504.01496 [hep-ph]].
- [18] M. Fabbrichesi, R. Floreanini and L. Marzola, “Local vs. nonlocal entanglement in top-quark pairs at the LHC,” *JHEP* **11**, 005 (2025) doi:10.1007/JHEP11(2025)005 [arXiv:2505.02902 [hep-ph]].
- [19] D. Gonçalves, A. Kaladharan, F. Krauss and A. Navarro, “Quantum entanglement is quantum: ZZ production at the LHC,” *JHEP* **12**, 122 (2025) doi:10.1007/JHEP12(2025)122 [arXiv:2505.12125 [hep-ph]].
- [20] A. Ruzi, Y. Wu, R. Ding and Q. Li, “Searching quantum entanglement in the  $pp \rightarrow ZZ$  process\*,” *Chin. Phys.* **50**, no.2, 023103 (2026) doi:10.1088/1674-1137/ae1374 [arXiv:2506.16077 [hep-ph]].
- [21] D. Gonçalves, A. Kaladharan and A. Navarro, “Higher-order corrections to quantum observables in  $h \rightarrow WW^*$ ,” *JHEP* **11**, 158 (2025) doi:10.1007/JHEP11(2025)158 [arXiv:2506.19951 [hep-ph]].
- [22] M. Del Gratta, F. Fabbri, M. Grossi, F. Maltoni, D. Pagani, G. Pelliccioli and A. Vicini, “Z-boson quantum tomography at next-to-leading order,” *JHEP* **02**, 056 (2026) doi:10.1007/JHEP02(2026)056 [arXiv:2509.20456 [hep-ph]].
- [23] T. Flacke, B. Fuks, D. Kim, J. Kim, S. J. Lee and L. Munoz-Aillaud, “New physics in toponium’s shadow?,” [arXiv:2512.03220 [hep-ph]].
- [24] L. Antozzi, E. Chalbaud, F. Déliot, F. Fabbri, M. C. N. Fiolhais, B. Fuks, A. Onofre, M. White and P. Zhu, “Extracting a Toponium Signal at the LHC with Spin and Quantum Information Tools,” [arXiv:2602.23426 [hep-ph]].
- [25] A. Hayrapetyan *et al.* [CMS], “Observation of a pseudoscalar excess at the top quark pair production threshold,” *Rept. Prog. Phys.* **88**, no.8, 087801 (2025) doi:10.1088/1361-6633/adf7d3 [arXiv:2503.22382 [hep-ex]].
- [26] [ATLAS], “Observation of a cross-section enhancement near the  $t\bar{t}$  production threshold in  $\sqrt{s} = 13$  TeV  $pp$  collisions with the ATLAS detector,” ATLAS-CONF-2025-008.
- [27] B. Fuks, K. Hagiwara, K. Ma, L. Munoz-Aillaud and Y. J. Zheng, “Prospects for toponium formation at the LHC in the single-lepton mode,” [arXiv:2509.03596 [hep-ph]].

- [28] F. Maltoni, C. Severi, S. Tentori and E. Vryonidou, “Quantum tops at circular lepton colliders,” JHEP **09**, 001 (2024) doi:10.1007/JHEP09(2024)001 [arXiv:2404.08049 [hep-ph]].
- [29] M. Fabbrichesi and L. Marzola, “Quantum tomography with  $\tau$  leptons at the FCC-ee: Entanglement, Bell inequality violation,  $\sin^2\theta_W$ , and anomalous couplings,” Phys. Rev. D **110**, no.7, 076004 (2024) doi:10.1103/PhysRevD.110.076004 [arXiv:2405.09201 [hep-ph]].
- [30] T. Han, M. Low and Y. Su, “Entanglement and Bell nonlocality in  $\tau^+\tau^-$  at the BEPC,” JHEP **10**, 217 (2025) doi:10.1007/JHEP10(2025)217 [arXiv:2501.04801 [hep-ph]].
- [31] Y. C. Guo, T. Han, M. Low and Y. Su, “Quantum Tomography of Fermion Pairs in  $e^+e^-$  Collisions: Longitudinal Beam Polarization Effects,” [arXiv:2602.02719 [hep-ph]].
- [32] E. Gabrielli and L. Marzola, “Quantum Entanglement and Bell Nonlocality at Future Lepton Collider,” [arXiv:2602.03960 [hep-ph]].
- [33] H. W. Zhang, X. Cao and T. F. Feng, “Manipulating Bell nonlocality and entanglement in polarized electron-positron annihilation,” [arXiv:2602.10389 [hep-ph]].
- [34] B. Yang, Y. Zhang, Z. S. Wang and X. Zhou, “Entanglement measures and Bell-type spin-correlation observables in tau-lepton pairs at the Super Tau-Charm Facility,” [arXiv:2603.05846 [hep-ph]].
- [35] R. Ding, A. Ruzi, S. Qian, A. Levin, Y. Wu and Q. Li, “Quantum Entanglement between gauge boson pairs at a Muon Collider,” [arXiv:2504.09832 [hep-ph]].
- [36] M. Del Gratta, F. Fabbri, P. Lamba, F. Maltoni and D. Pagani, “Quantum properties of  $H \rightarrow VV^*$ : precise predictions in the SM and sensitivity to new physics,” JHEP **09**, 013 (2025) doi:10.1007/JHEP09(2025)013 [arXiv:2504.03841 [hep-ph]].
- [37] M. Fabbrichesi, R. Floreanini, E. Gabrielli and L. Marzola, “Quantum-entangled pions,” Phys. Rev. D **112**, no.9, 9 (2025) doi:10.1103/PhysRevD.112.094009 [arXiv:2506.05464 [hep-ph]].
- [38] M. Fabbrichesi, R. Floreanini and L. Marzola, “About Witnessing Bell Non-locality at Colliders,” Found. Phys. **55**, no.6, 83 (2025) doi:10.1007/s10701-025-00894-7 [arXiv:2503.18535 [quant-ph]].
- [39] Y. Afik, F. Fabbri, M. Low, L. Marzola, J. A. Aguilar-Saavedra, M. M. Altakach, N. A. Asbah, Y. Bai, H. Banks and A. J. Barr, *et al.* “Quantum information meets high-energy physics: input to the update of the European strategy for particle physics,” Eur. Phys. J. Plus **140**, no.9, 855 (2025) doi:10.1140/epjp/s13360-025-06752-9 [arXiv:2504.00086 [hep-ph]].
- [40] I. F. Ginzburg, G. L. Kotkin, V. G. Serbo and V. I. Telnov, “Colliding gamma e and gamma gamma Beams Based on the Single Pass Accelerators (of Vlepp Type),” Nucl. Instrum. Meth. **205**, 47-68 (1983) doi:10.1016/0167-5087(83)90173-4
- [41] I. F. Ginzburg, G. L. Kotkin, S. L. Panfil, V. G. Serbo and V. I. Telnov, “Colliding gamma e and gamma gamma Beams Based on the Single Pass e+ e- Accelerators. 2. Polarization Effects. Monochromatization Improvement,” Nucl. Instrum. Meth. A **219**, 5-24 (1984) doi:10.1016/0167-5087(84)90128-5
- [42] J. H. Kuhn, E. Mirkes and J. Steegborn, “Heavy quark production at a photon linear collider,” Z. Phys. C **57**, 615-622 (1993) doi:10.1007/BF01561480
- [43] B. Badelek *et al.* [ECFA/DESY Photon Collider Working Group], “TESLA: The Superconducting electron positron linear collider with an integrated X-ray laser laboratory. Technical design report. Part 6. Appendices. Chapter 1. Photon collider at TESLA,” Int. J. Mod. Phys. A **19**, 5097-5186 (2004) doi:10.1142/S0217751X04020737 [arXiv:hep-ex/0108012 [hep-ex]].
- [44] D. Asner, H. Burkhardt, A. De Roeck, J. Ellis, J. Gronberg, S. Heinemeyer, M. Schmitt, D. Schulte, M. Velasco and F. Zimmermann, “Higgs physics with a gamma gamma collider based on CLIC I,” Eur. Phys. J. C **28**, 27-44 (2003) doi:10.1140/epjc/s2002-01113-3 [arXiv:hep-ex/0111056 [hep-ex]].
- [45] T. Barklow, C. Emma, Z. Huang, A. Naji, E. Nanni, A. Schwartzman, S. Tantawi and G. White, “XCC: An X-ray FEL-based  $\gamma\gamma$  Compton Collider Higgs Factory,” JINST **18**, no.07, P07028 (2023) doi:10.1088/1748-0221/18/07/P07028 [arXiv:2306.10057 [physics.acc-ph]].
- [46] H. Abramowicz *et al.* [Linear Collider Vision], “A Linear Collider Vision for the Future of Particle Physics,” [arXiv:2503.19983 [hep-ex]].
- [47] H. Abramowicz *et al.* [Linear Collider], “The Linear Collider Facility (LCF) at CERN,” [arXiv:2503.24049 [hep-ex]].
- [48] A. Peres, “Separability criterion for density matrices,” Phys. Rev. Lett. **77**, 1413-1415 (1996) doi:10.1103/PhysRevLett.77.1413 [arXiv:quant-ph/9604005 [quant-ph]].
- [49] W. K. Wootters, “Entanglement of formation of an arbitrary state of two qubits,” Phys. Rev. Lett. **80**, 2245-2248 (1998) doi:10.1103/PhysRevLett.80.2245 [arXiv:quant-ph/9709029 [quant-ph]].
- [50] J. F. Clauser, M. A. Horne, A. Shimony and R. A. Holt, “Proposed experiment to test local hidden variable theories,” Phys. Rev. Lett. **23**, 880-884 (1969) doi:10.1103/PhysRevLett.23.880
- [51] R. Horodecki, P. Horodecki and M. Horodecki, “Violating Bell inequality by mixed spin-1/2 states: necessary and sufficient condition,” Phys. Lett. A **200**, no.5, 340-344 (1995) doi:10.1016/0375-9601(95)00214-N
- [52] E. Asakawa, S. Y. Choi, K. Hagiwara and J. S. Lee, “Measuring the Higgs CP property through top quark pair production at photon linear colliders,” Phys. Rev. D **62**, 115005 (2000) doi:10.1103/PhysRevD.62.115005 [arXiv:hep-ph/0005313 [hep-ph]].
- [53] K. Hagiwara and D. Zeppenfeld, “Helicity Amplitudes for Heavy Lepton Production in  $e^+e^-$  Annihilation,” Nucl. Phys. B **274**, 1-32 (1986) doi:10.1016/0550-3213(86)90615-2
- [54] W. Bernreuther, D. Heisler and Z. G. Si, “A set of top quark spin correlation and polarization observables for the LHC: Standard Model predictions and new physics contributions,” JHEP **12**, 026 (2015) doi:10.1007/JHEP12(2015)026 [arXiv:1508.05271 [hep-ph]].